Diploma Thesis

Coupling Matrix based Bandpass Filter

performed at the

Institute of Electrodynamics, Microwave and Circuit Engineering
Technische Universität Wien

supervised by

Assoc. Prof. Dipl.-Ing. Dr. techn. Holger Arthaber
and
Univ. Ass. Dipl.-Ing. Bernhard Pichler, BSc.

by

Jure Soklič, dipl. inž. el. (UN)
Matr. Nr. 01432109

Vienna, November 16, 2018

Abstract

Bandpass filters are widely deployed in modern RF communication systems. The mathematical concepts of these filters, their characteristic functions, and coupling matrices were discussed by many authors. However, when realizing an actual 3-D filter structure, little information is available in literature. This thesis presents a step-by-step guide for the design of a resonant cavity based filter. It starts from a coupling matrix, continues with the simulation of 3-D models and works its way up to manufacturing the filter. The design is optimized for in-house production, considering limits of the available machines and materials. Therefore, the designed filter is not optimal from its electrical characteristics, however critical parameters can be determined. Additionally, two common techniques for loss reduction, i.e. polishing and silver-plating, are experimentally evaluated. To do so, a simple resonant cavity is designed. To determine the influence on the losses, the unloaded quality factor was estimated. Therefore, two common quality estimation methods were applied on the cavity, utilizing different energy coupling mechanisms. However, these did not show the desired accuracy. Consequently, a new method is developed, which considers coupling mechanism imperfections. Polishing was found to give a negligible loss reduction, while silver-plating indicates a quality factor improvement of 33%. Hence, silver-plating was also applied to the filter in order to reduce the losses. With this technique, a filter was designed with a very low insertion loss, which fits the requirements of the design. Furthermore, this was achieved with minimized manufacturing effort, allowing to build it with simple machines.

Kurzfassung

In Kommunikationssystemen sind Bandpass Filter ein unersetzbarer Bestandteil. Die mathematischen Konzepte dahinter, wie Eigenfunktionen und Kopplungsmatrizen, sind in der Literatur detailliert beschrieben. Wie man diese mathematischen Konzepte in eine 3D-Filter-Struktur umsetzt, ist hingegen kaum dokumentiert. In dieser Arbeit wird eine Schritt-für-Schritt Anleitung für den Entwurf und die Herstellung eines Bandpass Filters präsentiert. Dabei wird mit der Kopplungsmatrix-Synthese gestartet, daraus eine 3D Simulation des Filters durchgeführt und zuletzt das Filter gefertigt. Ziel dieser Arbeit ist es, dieses Filter in Eigenfertigung zu realisieren, da heißt eine Anpassung der Filtergeometrie an den Fertigungsprozess. Die elektrischen Eigenschaften werden somit nicht optimal sein, jedoch ist es Ziel der Arbeit die kritischen Parameter zu identifizieren. Zusätzlich werden zwei Techniken zur Reduzierung der Verluste eingesetzt: Oberflächenpolitur und Versilberung. Der Effekt soll anhand eines einfachen Resonators gezeigt werden. Dazu muss die Güte bestimmt werden, wofür zwei aus der Literatur bekannte Methoden verwendet wurden. Der Resonator wurde dazu mit unterschiedlichen Kopplungen gemessen. Da diese beiden Methoden unzureichende Ergebnisse lieferten, wurde eine neue Methode entwickelt, die die Verluste in den Kopplungsmechanismen berücksichtig, was eine genauere Gütebestimmung bewirkt. Es hat sich gezeigt, dass Oberflächenpolitur die Güte nur unwesentlich verbessert, jedoch eine Versilberung der Oberfläche bewirkt eine Erhöhung der Güte um 33%. Deshalb wurde auch die Oberfläche des Filters versilbert. Somit wurde ein Bandpass Filter mit sehr kleiner Einfügedämpfung erzeugt, was den Anforderungen voll und ganz entspricht. Dies wurde erreicht mit minimalem Fertigungsaufwand, wodurch dieses Filter nur mit einfachen Maschinen gefertigt werden konnte

Acknowledgements

I would like to thank my thesis advisor, Assoc. Prof. Dr. techn. Holger Arthaber, for his constant support and guidance. With his knowledgeableness, he has steered me in the right direction throughout the research and writing of this work.

For all the advice and help they have provided, I would also like to thank all the members of the Microwave Engineering Group at TU Wien, especially Project Ass. Dipl.-Ing. Michael Zaisberger and Univ. Ass. Dipl.-Ing. Bernhard Pichler. In times of doubt, I could always turn to them for guidance.

Last but not least, I would like to express my gratitude and eternal indebtedness to my parents. Without their constant unlimited support throughout my academic path, this achievement would be unreachable.

Table of Contents

List of Figures

List of Tables

Abbreviations

BPF bandpass filter

CST Computer Simulation Technology

EM electromagnetic

FD3D Filter Designer 3D

FIR frequency-invariant response

MSE mean squared error

MW microwave

PEC perfect electric conductor

Q-factor quality factor

$\mathbf{Q_{ext}}$ external quality factor

$\mathbf{Q_L}$ loaded quality factor

$\mathbf{Q_0}$ unloaded quality factor

RF radio frequency

TE transverse electric

TEM transverse electromagnetic

TM transverse magnetic

VNA vector network analyzer

1 Introduction

Microwave filters represent one of the basic building blocks for any modern-day telecommunication system. As such, they have been a topic of great interest in the radio frequency (RF) engineering community in both the current and the previous century. Various mathematical models have been derived for the design and computation of filter elements, giving different filter behaviors, e.g. steep passband-to-stopband transition (Chebyshev) filter, the maximally flat (Butterworth) filter, or more complex filters introducing transmission zeros [1, Ch. 3]. In the early 1970s, the term filter coupling matrix was introduced, which represents a filter as a cascade of resonators with coupling coefficients between all pairs of resonators, as explained in [1, Ch. 8]. This allows for the use of matrix operations, substantially simplyfing the synthesis procedure required for the design of filters.

With the technological advances in the computer technology, 3-D electromagnetic (EM) simulation software became commercially available in the last decades of the previous century. Such software enables a designer to simulate the designed RF component before the actual production, to observe if the behavior conforms to what is expected and, if necessary, to adapt appropriately, thus reducing the total costs and time required for the design. Additionally, various software also provides numerous optimization algorithms, which can be used to modify the design parameters in order to reach the desired design goal. It is worth noting, however, that these optimization processes are both resource and time demanding and should only be used when the design is already close to the design goals.

The main goal of this thesis is to design and produce a narrowband bandpass filter (BPF), operating in the L-band. It is intended to be used in an aircraft communication system, operating at a channel with a frequency range from 963.5 MHz to 970.5 MHz. To avoid interference from the neighboring channel, which is placed at the frequency band above this one, strong stopband rejection for this band is required. To do so, a box section model [1, Ch. 10, Sec. 4] is used, which allows for nonsymmetric transmission parameters with one or more transmission zeros. The initial filter design can be seen below, in Figure 1.1. With the help of Computer Simulation Technology (CST) Microwave Studio [2], a 3-D EM simulation software, separate filter segments as well as the complete filter are simulated and adapted accordingly. The goal is to produce the designed filter in-house, using machines with limited precision, recognizing the tolerances of the filter to this limited precision and identifying the critical parameters. As a consequence, an optimum filter structure in the sense of filter performance is not possible. Instead, it is optimized to the manufacturing process, using materials which are easily available and easy to process. An aluminum alloy was used for the structures which have to be milled and brass was used for the structures which require hollowing by a turning machine. Concretely, the aluminum alloy is AlMgSi0,5, while the composition of the brass is unfortunately unknown. The materials used would be sub-optimum if designing an optimal filter, however, the main goal is to get acquainted with the design process and see if it is possible to manufacture such a filter with the available equipment. Beside the non-optimum materials, many design parameters are optimized for the manufacturing process as well.

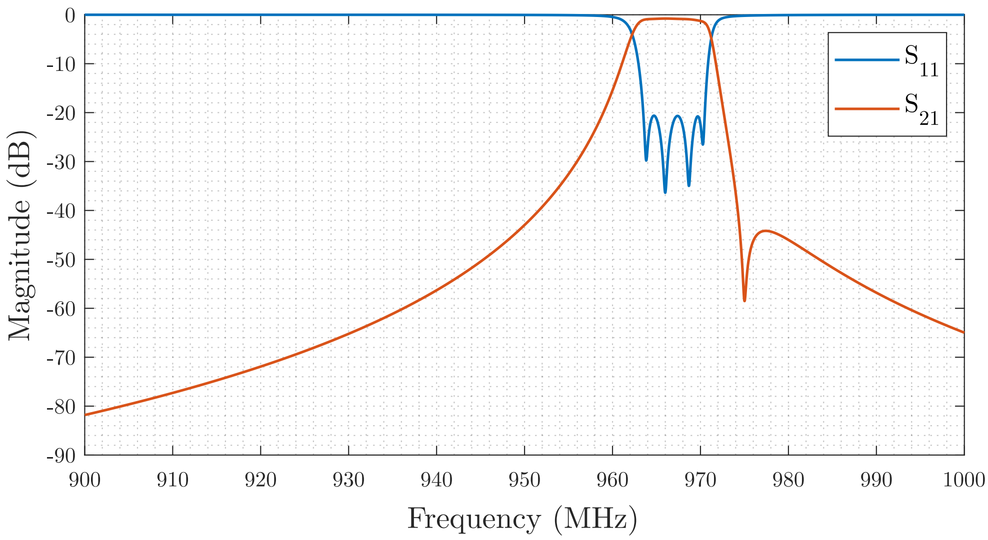

Figure 1.1: Initial filter design: S-parameters

Furthermore, two common techniques are used to improve the quality of the filter, i.e. surface polishing and silver-plating. Using a resonant cavity, these techniques are evaluated in order to obtain quantitative information about their effect and compare the results with the theoretically obtained expected values. To do so, it is required to obtain the unloaded quality factor (Q_0) [3]. To minimize the effects of imperfections caused by the production process, a simplified cylindrical cavity is to be used. A new method for determining Q_0 is implemented, using an error minimization algorithm and the equivalent circuit model of a resonant cavity.

Designing a practical model generally lacks literature support, while the existing literature offers many empirical formulae. The document aims to provide the reader with a step-by-step guide to design and produce a microwave resonant cavity filter with limited tools available. Its goal is to simplify and speed up the process of designing an RF BPF for the reader. It also provides quantitative results for the techniques used to improve the overall quality of the filter, which should help the reader decide whether to implement these methods in his/her given situation.

2 Microwave Filters

This chapter provides the theoretical background, necessary for conducting the design, production, and measurements described hereafter. Its intention is to make the reader familiar with the existing literature and the concepts used in this thesis. It is divided into six major sections, discussing the resonant cavities, which are the basic building blocks of any microwave filter, the evaluation of their losses with the help of a quality factor, coupling of energy to and between the resonators, the mathematical concepts for filter design, the physical realization of the mathematical model of a filter, and the common methods to reduce losses in microwave (MW) filters.

Section 2.1 introduces MW resonators. Different resonant structure topologies are presented along with the general definition of the quality factor (Q-factor) of a resonator and mathematically derived models for determining the quality factor of the resonant structures of interest. In addition, a simple equivalent circuit model for these structures is presented. Transporting energy to/from a resonator and between a pair of resonators is called energy coupling. It is a fundamental operation of any resonant MW structure. Both concepts are explained in Section 2.2. In Section 2.3, two methods of measuring the Q-factor are explained. An extended RLC circuit model including the mechanism to couple the energy into the resonator is considered. The two common methods of reducing losses in resonant structures are presented Section 2.4. Analytical models for a single resonator are given for both. The mentioned sections summarize all the concepts required for designing a filter. The actual mathematical synthesis of a filter is discussed in Section 2.5. Characteristic filter functions are presented and the concept of transmission zeros introduced. The main focus is put on the coupling matrix synthesis approach, which contains the resonator frequencies and the couplings between all resonator pairs. The last section, Section 2.6, continues with the selected filter model and its coupling matrix. It discusses the physical realization of the values obtained from the coupling matrix.

2.1 Microwave Resonators

The basic building block of any microwave filter is a resonator. EM resonators are capable of storing electric and magnetic energy. At resonance frequency, the two stored energy contributions are equal [1, Ch. 11]. Based on their topology, they can be grouped into three categories: lumped-element LC resonators, planar resonators, and three-dimensional cavity-type resonators.

2.1.1 Quality Factor (Q)

The most important parameter of a resonant circuit is its quality factor, Q [4, Ch. 6], defined as

$$Q = \omega \frac{\textit{average energy stored}}{\textit{energy loss/second}} = \omega \frac{W_m + W_e}{P_{loss}}. \tag{2.1}$$

It is a dimensionless quantity and indicates the amount of losses in the resonant cavity, rising towards infinity as the losses are decreasing towards zero. Equation (2.1) represents a general equation for the Q-factor. Based on the origin of the losses, different Q-factors can be derived. The loaded quality factor (Q_L) represents the quality factor of the overall system, which includes coupling mechanisms. These will be discussed in Section 2.2. It can be split into two contributions, one due to the losses in the resonant structure, Q_0, and one due to the losses in the coupling mechanism, called external quality factor (Q_{ext}).

When comparing resonators with different topologies, considering the same resonant frequency, both the size and Q_0 of the resonator increase in the same order. LC resonators have the smallest size and lowest Q_0, while 3-D structures result in the largest resonators with the highest Q_0 values. Thus, the selection of the resonator type is a trade-off between the dimensions and Q_0, which directly affects the insertion loss of a structure. The LC resonators have typical Q_0 values between 10 and 50 at 1 GHz, planar resonators are slightly better with a Q_0 between 50 and 300 at the same frequency, while 3-D structures offer values ranging from 3000 to 30 000 [1, Ch. 11]. Due to the high Q_0, needed to maintain the insertion loss low, the focus of this thesis will be only on the 3-D structures. Numerous 3-D resonant structures exist, the more common among them are the coaxial resonator, the rectangular and cylindrical waveguide cavity resonators, and dielectric resonators. Typically, the coaxial resonators are the smallest and the waveguide cavity resonators tend to be the largest for the same frequency of resonance. Coaxial resonators and cylindrical waveguide resonators are presented more thoroughly in the following two subsections. Both have an infinite number of resonant frequencies, each supported by a different propagation mode.

2.1.2 Coaxial Resonators

Coaxial resonators belong to the group of transmission-line resonant circuits, along with microstrip transmission-line resonators. Typically, transmission-line resonators are terminated in either a short or an open circuit [4, Ch. 6]. A resonator can be realised as a short-circuited $\lambda/2$ line, where the voltage wave at both ends is 0 for the resonant frequency, an open-circuited $\lambda/2$ line, where the voltages are at its peak at both ends, and a short-circuited $\lambda/4$ line, which has a maximum voltage at the open side and zero voltage at the short-circuited side. Based on the frequency dependent dimensions of all these resonators, the size for a $\lambda/4$ resonator is half of that for any of the $\lambda/2$ realizations. The unloaded Q-factor, Q_0, for the fundamental transverse electromagnetic (TEM) mode of such a resonator is given in [5, Ch. 5] as

$$Q_0 = \frac{\lambda}{\delta} \frac{1}{4 + \frac{2L}{a} \cdot \frac{1+a/b}{ln(a/b)}}, \tag{2.2}$$

where δ is the skin depth, L the length of the resonator, and a and b the outer and inner diameter of the coaxial resonator. The equation is given for a half-wavelength resonator, hence the 2L dependence in the denominator. A general practical form is given later in Equation (2.66). We should note here, that beside the influence of the skin depth, the ratio between the diameters plays an important role in determining Q_0. Concretely, a ratio of $a/b = 3.6$ is found to be the optimal ratio, giving the maximum Q_0.

2.1.3 Cylindrical Waveguide Resonators

Cylindrical resonant cavities can be considered as a section of a circular waveguide, shorted at both ends [4, Chs. 3, 6]. The cylindrical geometry of the resonant cavity supports transverse electric (TE) and transverse magnetic (TM) modes of propagation. To calculate the resonance frequencies of the modes, two equations are given. The equation for TE modes is given as

$$f_{nml(TE)} = \frac{c}{2\pi\sqrt{\mu_r\epsilon_r}}\sqrt{\left(\frac{p'_{nm}}{a}\right)^2 + \left(\frac{l\pi}{d}\right)^2}, \tag{2.3}$$

and the equation for TM modes as

$$f_{nml(TM)} = \frac{c}{2\pi\sqrt{\mu_r\epsilon_r}}\sqrt{\left(\frac{p_{nm}}{a}\right)^2 + \left(\frac{l\pi}{d}\right)^2}. \tag{2.4}$$

In the equations, a corresponds to the radius of the cavity, and d to the height of the cavity. Variables n, m, and l correspond to the number of circumferential (ϕ), radial (ρ), and longitudinal (z) variations respectively, indicating the number of field maxima in each of the cylindrical coordinates. The one variable in which the two equations differ is p'_{nm}, which is replaced by p_{nm} in the second equation. The values represent the m-th root of the derivative of the Bessel function of first kind, $J'_n(p'_{nm})$, and the m-th root of the Bessel function of first kind, $J_n(p_{nm})$, respectively. They represent the solution to the wave equation for a cylindrical cavity. The first 9 values for both variables are given in Table 2.1, starting with $m = 1$, to conform to the boundary conditions on the cavity surface. The same applies in z direction, leading to the lowest value and therefore the lowest TE mode being TE_{111}. For the TM mode, only the constraint in ρ direction applies, resulting in the lowest TM mode of a cylindrical cavity being TM_{010}.

n	p'_{n1}	p'_{n2}	p'_{n3}
0	3.832	7.016	10.174
1	1.841	5.331	8.536
2	3.054	6.706	9.970

n	p_{n1}	p_{n2}	p_{n3}
0	2.405	5.520	8.654
1	3.832	7.016	10.174
2	5.135	8.417	11.620

Table 2.1: Roots of $J'_n(p'_{nm})$ (left) and $J_n(p_{nm})$ (right)

An analytical expression for Q_0 of a cylindrical cavity exists as well, derived from the electric and magnetic field distributions within the cavity [6, Ch. 7]. For the sake of brevity, the derivation of the expression is omitted at this point. The analytical expression for the quality of TE modes is given as

$$Q_0 = \left(\frac{1}{Q_d} + \frac{1}{Q_c}\right)^{-1}. \tag{2.5}$$

Q_d is the contribution due to the dielectric material inside the cavity,

$$Q_d = \frac{1}{tan\ \delta}, \tag{2.6}$$

where $tan\ \delta$ is the loss tangent of the dielectric. Q_c is the contribution due to the losses in the imperfectly conducting walls,

$$Q_c = \frac{\lambda_0}{\delta_s} \frac{\left[1 - \left(\frac{n}{p'_{nm}}\right)^2\right]\left[\left(p'_{nm}\right)^2 + \left(\frac{l\pi a}{d}\right)^2\right]^{3/2}}{2\pi\left[\left(p'_{nm}\right)^2 + \frac{2a}{d}\left(\frac{l\pi a}{d}\right)^2 + \left(1 - \frac{2a}{d}\right)\left(\frac{nl\pi a}{p'_{nm} d}\right)^2\right]}, \tag{2.7}$$

where $\delta_s = 1/\sqrt{\pi f \mu_0 \sigma}$ is the skin depth and σ represents the electrical conductivity of the conducting walls.

2.1.4 Equivalent Parallel Lumped Elements RLC Circuit

The basic function of both presented types of resonators can conveniently be represented by a simple parallel RLC circuit, as the one shown in Figure 2.1. Since a resonant cavity

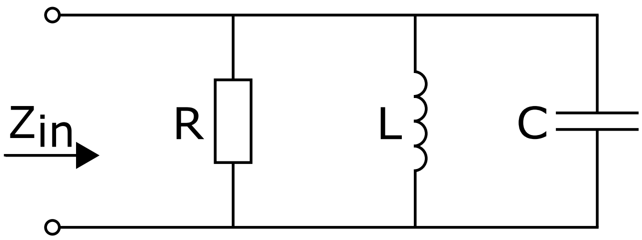

Figure 2.1: Equivalent lumped elements RLC circuit

produces an infinite number of resonant frequencies, it is worth noting here, that this model is only (approximately) accurate around a certain resonant frequency and, additionally, disregards the mechanism used to couple the energy to the resonant cavity. The input impedance of the model is

$$Z_i = \left(\frac{1}{R} + \frac{1}{j\omega L} + j\omega C\right)^{-1}, \tag{2.8}$$

and the complex power delivered to the resonator is

$$P_i = \frac{1}{2} V I^* = \frac{1}{2}|V|^2 \frac{1}{Z_i^*} = \frac{1}{2}|V|^2 \left(\frac{1}{R} + \frac{j}{\omega L} - j\omega C\right), \tag{2.9}$$

as described in [4, Ch. 6]. If the contributions are separated to the power dissipated by the resistor, the average electric energy stored in the capacitor and the average magnetic energy stored in the inductor, the complex power can be rewriten as

$$P_i = P_{loss} + 2j\omega(W_m - W_e), \tag{2.10}$$

where

$$P_{loss} = \frac{|V|^2}{2R}, \qquad W_m = \frac{|V|^2}{4\omega^2 L}, \qquad \text{and} \qquad W_e = \frac{|V|^2 C}{4}. \tag{2.11}$$

As mentioned before, the time-average stored magnetic and electric energies are equal in magnitude at a resonant frequency. However, the power contributions are 180° out of phase and cancel each other out, resulting in a purely real input impedance of R. From this condition and Equation (2.11), the resonant frequency can be defined as

$$\omega_0 = \frac{1}{\sqrt{LC}}. \tag{2.12}$$

2.2 Energy Coupling

Filters are typically built using multiple resonators, requiring the energy to be coupled between them. Moreover, even when speaking of a single resonator, the energy needs to be provided to the resonator and we can also talk about energy coupling. In general, the coupling coefficient is defined as the ratio of coupled energy to stored energy [7]. In integral form, this can be described as

$$\kappa = \frac{\iiint \varepsilon \mathbf{E_1} \cdot \mathbf{E_2} \, \mathrm{d}v}{\sqrt{\iiint \varepsilon |\mathbf{E_1}|^2 \, \mathrm{d}v \cdot \iiint \varepsilon |\mathbf{E_2}|^2 \, \mathrm{d}v}} + \frac{\iiint \varepsilon \mathbf{H_1} \cdot \mathbf{H_2} \, \mathrm{d}v}{\sqrt{\iiint \varepsilon |\mathbf{H_1}|^2 \, \mathrm{d}v \cdot \iiint \varepsilon |\mathbf{H_2}|^2 \, \mathrm{d}v}}, \tag{2.13}$$

where the contribution of the electrical fields (electric coupling) and the magnetic fields (magnetic coupling), evaluated at resonance, are summed up to give the total coupling. The coupling can either be positive or negative, which corresponds to either enhancing or reducing the stored energy. Moreover, the electric coupling and the magnetic coupling can be of opposite signs, causing the opposite effect on the stored energy. In Figure 2.2, a graphical representation of the coupling is given. Note that the structure and the self-resonant frequency of the two resonators can be different. Also, the coupling mechanism to transport the energy to a resonator can be considered as a resonator itself, thus making Equation (2.13) generally applicable. Since this method requires known field distributions

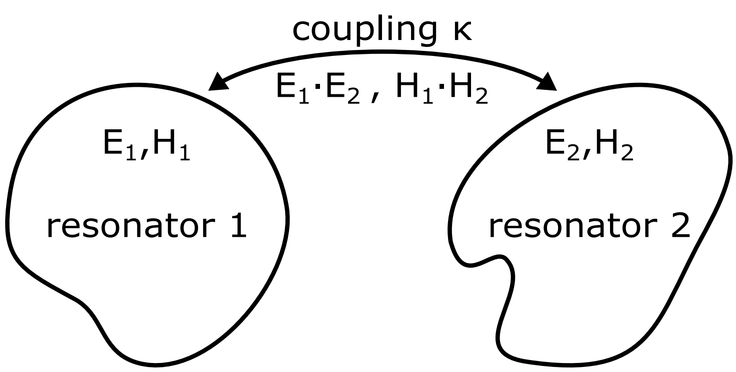

Figure 2.2: General coupled microwave resonators

and integration over space, it is generally a very complex procedure. Instead, the goal is to find characteristic frequencies related to the electric and magnetic coupling. Using lumped element circuits, Hong derives the coupling coefficient equation based on four characteristic frequencies [7]. These are the uncoupled resonant frequencies of both the resonators, ω_{01} and ω_{02}, and the two resonant frequencies of the complete system, ω_1 and ω_2. The equation is then defined as

$$\kappa = \pm\frac{1}{2}\left(\frac{\omega_{02}}{\omega_{01}} + \frac{\omega_{01}}{\omega_{02}}\right) \cdot \sqrt{\left(\frac{\omega_2^2 - \omega_1^2}{\omega_2^2 + \omega_1^2}\right)^2 - \left(\frac{\omega_{02}^2 - \omega_{01}^2}{\omega_{02}^2 + \omega_{01}^2}\right)^2}, \tag{2.14}$$

In [8, Ch. 8], Hong further suggests that the meaning of positive or negative coupling in filter design is relative. Coupling of energy occurs due to reactive elements. If a certain S-parameter phase response of a coupling is considered to represent the positive coupling, the coupling with opposite phase response sign represents the negative coupling. However, by convention, capacitive couplings are considered negative, while inductive couplings are considered positive. When constructing a filter, each is realized with a different mechanism. The mechanisms will be presented in Section 2.6.

External Coupling

External coupling represents the input/output coupling of energy to/from the resonator with the use of a coupling mechanism. The maximum power transfer between the external circuitry and the resonator is achieved when the coupling coefficient, κ, is one. In this case, the resonator is matched to the feed line of the external circuit, and is said to be critically coupled [4, Ch. 6]. The coupling coefficient can be expressed as

$$\kappa = \frac{Q_0}{Q_{ext}}. \tag{2.15}$$

When $\mathrm{Q_0}$ is larger than $\mathrm{Q_{ext}}$, the resonator is said to be overcoupled, giving $\kappa > 1$. If $\mathrm{Q_0}$ is smaller than $\mathrm{Q_{ext}}$, the resonator is said to be undercoupled. The coupling coefficient in that case is $\kappa < 1$. The level of required coupling depends on the application. The coupling coefficient plays an important role when measuring $\mathrm{Q_0}$, which will be discussed further in the next section.

2.3 Measuring Unloaded Q-Factor

The unloaded Q-factor is the characteristic of interest, as it allows for an evaluation of the resonant cavity properties. In a realistic setup, however, $\mathrm{Q_0}$ cannot be directly measured. The losses in the coupling mechanism circuitry lower its value to the value of the overall, loaded Q-factor, $\mathrm{Q_L}$. Various methods have been devised for the extraction of $\mathrm{Q_0}$ from the measurements, both one- and two-port [1, Ch. 11]. The first methods were created before the vector network analyzers (VNAs) became widely spread, which is the case nowadays. These methods were gathered and described by Ginzton in [9, Chs. 9, 10].

Kajfez and Hwan proposed the first method using a VNA in [3]. An equivalent resonant circuit in a wide frequency band is offered for the resonant cavity, comprising of an infinite series of resonant circuits (as the one seen in Figure 2.1), each representing one resonant mode of the cavity. The coupling of energy is represented with an additional impedance.

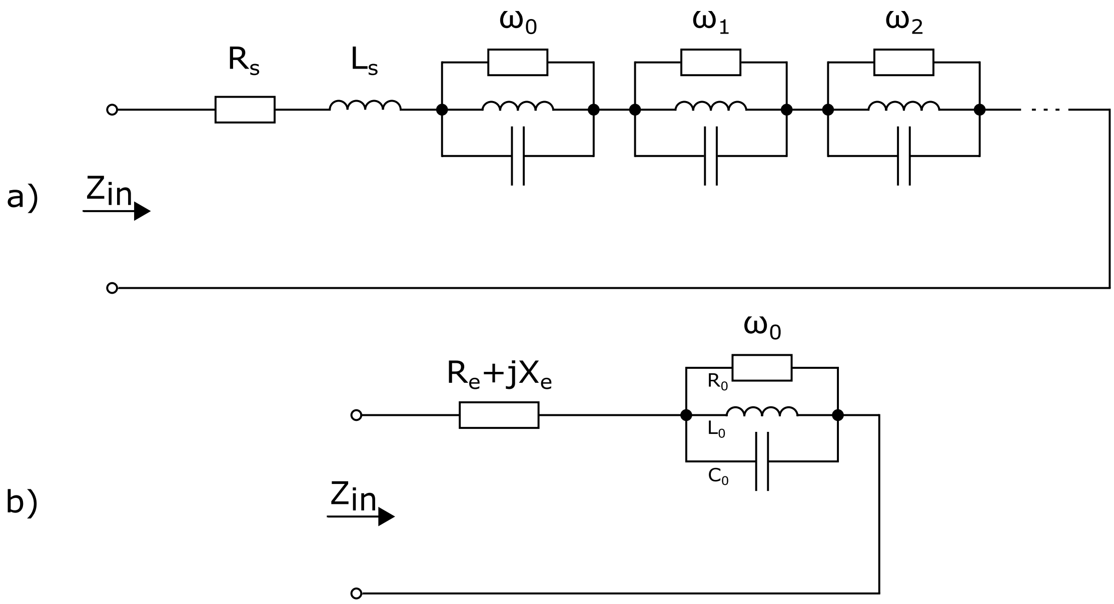

Figure 2.3: Resonant cavity equivalent circuit model: a) full model; b) simplified equivalent circuit in the vicinity of resonant frequency ω_0

In Figure 2.3(a), the cavity is inductance-coupled, therefore an inductor L_s represents the reactive part of the coupling impedance. When near to a certain resonant frequency, the circuit can be simplified to the one shown in Figure 2.3(b). The "external impedance", $R_e + jX_e$, is now a combination of the contributions due to the coupling mechanism and the contributions due to other resonant circuits. The resistive component is ignored, while the reactance component is presented with the first two terms of a Taylor series as

$$X_e = X_1 + 2Z_0Q_1\psi, \tag{2.16}$$

where X_1 is the constant reactive part, Z_0 the characteristic impedance of the transmission line to which the circuit is connected, Q_1 the linearly growing part and ψ (the authors use δ, which is already used in this document for the skin effect) is the frequency detuning parameter, defined as follows

$$\psi = \frac{\omega - \omega_0}{\omega_0}. \tag{2.17}$$

In the whole range of used frequencies, which are close to the resonant frequency, $|\psi| \ll 1$, and we can approximate

$$\frac{\omega}{\omega_0} - \frac{\omega_0}{\omega} \simeq 2\psi. \tag{2.18}$$

When considering the lowest resonant frequency, ω_0, and neglecting the presence of higher resonant frequencies, the function X_e (when inductively coupled) becomes

$$X_e = \omega_0 L_e(1 + \psi) = X_1(1 + \psi), \tag{2.19}$$

and the input impedance of the circuit, Z_i is then

$$Z_i = jX_e + \frac{R_0}{1 + jQ_0\left(\frac{\omega}{\omega_0} - \frac{\omega_0}{\omega}\right)} = jX_1(1 + \psi) + \frac{R_0}{1 + j2Q_0\psi}. \tag{2.20}$$

The input reflection coefficient is then

$$\Gamma_i = \frac{Z_i - Z_0}{Z_i + Z_0} = \frac{Z_F - Z_S^*}{Z_F + Z_S}, \tag{2.21}$$

where the impedance is separated in a fast varying function, Z_F, and a slow varying function, Z_S. The slow varying elements of the impedance are

$$Z_S = Z_0 \left[1 + j \left(\frac{X_1(1+\psi)}{Z_0} \right) \right], \tag{2.22}$$

and the resonant circuit contributes to the fast varying elements

$$Z_F = \frac{R_0}{1 + j2Q_0\psi}. \tag{2.23}$$

When the frequency is detuned (offset from the resonant frequency), the fast varying function is negligible and the input reflection coefficient is

$$\Gamma_D = -\frac{Z_S^*}{Z_S}, \tag{2.24}$$

and the difference $\Gamma_i - \Gamma_D$ takes the form

$$\Gamma_i - \Gamma_D = \frac{2Z_0}{Z_S^2 \left(Z_S^{-1} + Z_F^{-1}\right)} \simeq \frac{2Z_0}{Z_S^2 \left(\frac{1}{Z_0} \left(\frac{1}{1+x_1^2} + \frac{Z_0}{R_0} \right) (1 + j2Q_L\psi_L) \right)}. \tag{2.25}$$

Here, x_1 is the normalized reactance, ψ_L the loaded detuning parameter, defined as

$$\psi_L = \frac{\omega - \omega_L}{\omega_0} = \psi - \frac{x_1\kappa}{2Q_0}, \tag{2.26}$$

and the loaded Q factor, Q_L, as

$$Q_L = \frac{Q_0}{1+\kappa}. \tag{2.27}$$

The variable κ in the last two equations is the coupling coefficient

$$\kappa = \frac{R_0}{Z_0(1+x_1^2)}. \tag{2.28}$$

The ψ dependence in Equation (2.22) is now neglected and Z_S^2 approximated as

$$Z_S^2 = Z_0 \left(1 + x_1^2\right) e^{j2tan^{-1}x_1}, \tag{2.29}$$

which, inserted in Equation (2.25), gives

$$\Gamma_i - \Gamma_D = \frac{2e^{j2tan^{-1}x_1}}{(1+\kappa^{-1})\,(1 + j2Q_L\psi_L)}. \tag{2.30}$$

This equation describes a circle on a Smith chart, an example is presented in Figure 2.4. The maximum absolute value of the equation gives the diameter of the circle. The loaded detuning parameter, ψ_L, in this case is zero, allowing to express the diameter of the circle

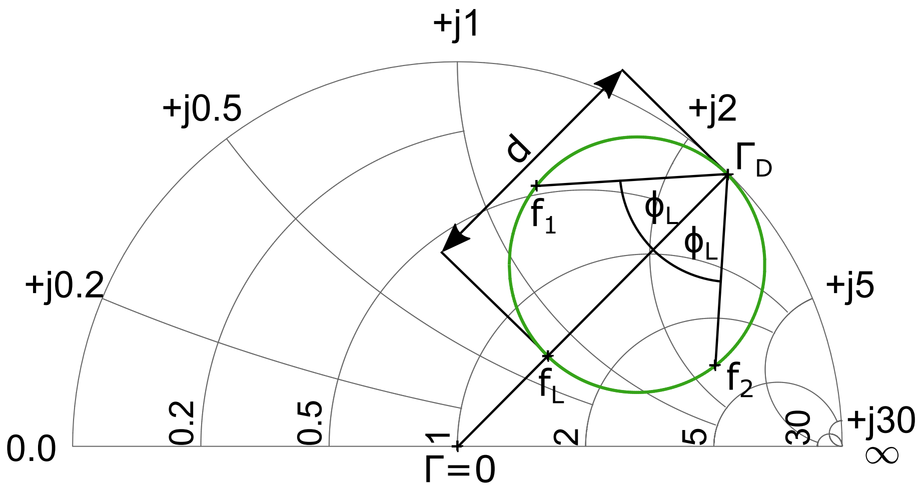

Figure 2.4: Example of the circle described by $\Gamma_i - \Gamma_D$ in Smith chart

just with the coupling coefficient. After rearranging, the value of κ based on the diameter of the circle is found to be

$$\kappa = \frac{d}{2-d}. \tag{2.31}$$

The loaded Q-factor can also be expressed from Equation (2.30). The only variable that changes when changing the frequency ψ_L is the angle ϕ_L, marked in Figure 2.4 is expressed by

$$tan\phi_L = -2Q_L\psi_L, \tag{2.32}$$

from which the formula for Q_L follows

$$Q_L = \frac{f_0}{f_{(+\phi_L)} - f_{(-\phi_L)}} tan\phi_L \simeq \frac{f_L}{f_1 - f_2} tan\phi_L, \tag{2.33}$$

where f_L is assumed to be approximately equal to f_0. Finally, Q_0 is obtained from Equation (2.27) as

$$Q_0 = Q_L(1+\kappa), \tag{2.34}$$

Another method for evaluation of Q_0 was proposed by Shahid et al. [10]. The authors propose a simple and fast method which makes use of two least square algorithms applied sequentially. The method is derived using the same circuit model as in the previous method, shown in Figure 2.3(b), therefore the input impedance derivations apply here as well. In the first step, a circle is fitted to the measured reflection parameter data using the circle fitting procedure described in [11]. The diameter of the fitted Q-circle can then be used in Equation (2.31) to obtain the coupling coefficient κ. The authors define the input reflection function as

$$\Gamma_i = \Gamma_D \left[\frac{(1-\kappa)/(1+\kappa) + j2Q_L\psi_L}{1 + j2Q_L\psi_L} \right], \tag{2.35}$$

where the detuned reflection coefficient is

$$\Gamma_D = \frac{jX_e - Z_0}{jX_e + Z_0} = e^{j\phi_D}, \tag{2.36}$$

and is considered to have unit magnitude. At resonance, the detuning parameter is zero and the loaded reflection coefficient is expressed as

$$\Gamma_L = \Gamma_D \left(\frac{1-\kappa}{1+\kappa}\right), \tag{2.37}$$

If $\kappa > 1$, the Q-circle encloses the center of the Smith chart and $\angle\Gamma_L = \phi_L = \phi_D + \pi$, and otherwise $\phi_L = \phi_D$. From Equations (2.35) and (2.37) the following expression can be obtained

$$2Q_L\psi_L = -\left[\frac{j(\Gamma_i - \Gamma_L)}{\Gamma_D - \Gamma_i}\right], \tag{2.38}$$

which is interpreted trigonometrically as shown in Figure 2.5. The three points, Γ_i, Γ_D, and Γ_L, build a triangle with a right angle between $|\Gamma_i - \Gamma_L|$ and $|\Gamma_D - \Gamma_i|$. Since $\Gamma_i - \Gamma_L$ is multiplied with j, the resulting ratio in Equation (2.38) is always a real value, the tangent of the angle ϕ_i. Hence, the equation translates to

$$2Q_L\psi_L = -tan\phi_i, \tag{2.39}$$

which is the basis for the linear frequency scale and the starting point for the second least squares algorithm. The error function is defined as

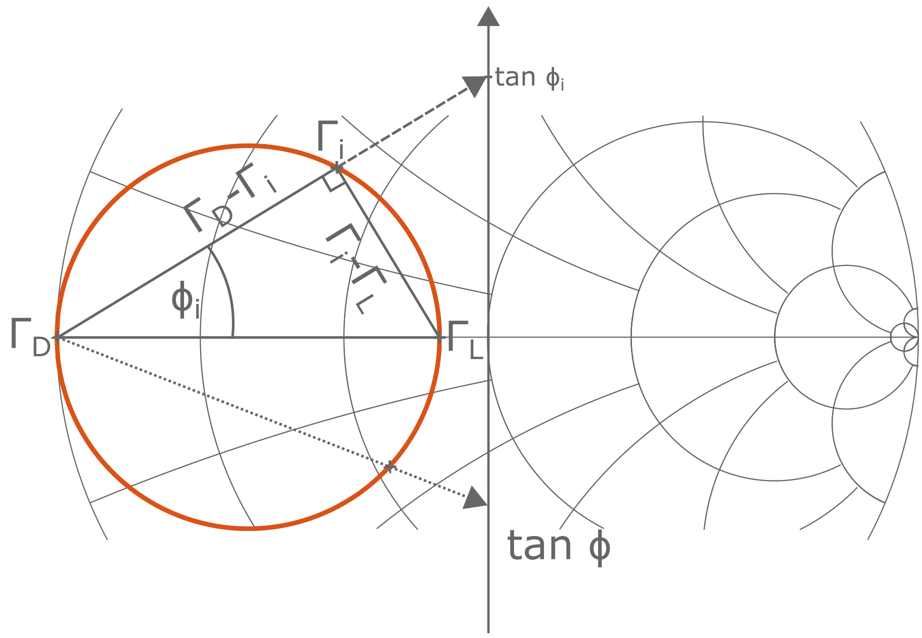

Figure 2.5: Trigonometric interpretation of the reflection coefficients

$$E = \sum_{in=1}^{N}\left[tan\phi_i + \frac{2Q_L}{f_0}(f_i - f_L)\right]^2 = \sum_{i=1}^{N}[y_i - (mx_i + c)]^2, \tag{2.40}$$

m being the slope and c the intercept of the least squares best straight line fit to xy data, x representing the frequency axis and y the $tan\phi_i$ axis. The normal equations for the two parameters are

$$m = \frac{N(\sum x_i y_i) - (\sum x_i)(\sum y_i)}{N(\sum x_i^2) - (\sum x_i)^2}, \tag{2.41}$$

and

$$c = \frac{(\sum y_i)(\sum x_i^2) - (\sum x_i y_i)(\sum x_i)}{N(\sum x_i^2) - (\sum x_i)^2}. \tag{2.42}$$

The parameters of interest can then be calculated from the two factors as

$$Q_L = \frac{c}{2}\frac{f_0}{f_L} - \frac{X_e}{2Z_0}\left(\frac{\kappa}{1+\kappa}\right) \simeq \frac{c}{2} - \frac{X_e}{2Z_0}\left(\frac{\kappa}{1+\kappa}\right) \simeq \frac{c}{2}, \tag{2.43}$$

and

$$f_L = -\frac{c}{m}. \tag{2.44}$$

The first Q_L approximation is made due to the fact that the loaded and unloaded resonant frequencies are typically very close and their ratio is therefore close to unity. X_e can be obtained from Equation (2.36). Typically, the second part of the equation for Q_L is much smaller than the first value, giving reason for the second approximation. Q_0 is calculated from Equation (2.34).

2.4 Q_0 Improvement Techniques

As explained earlier, Q_0 is a representation of the amount of losses in a MW structure. Since receivers require a certain level of power from the received signal and signal amplifiers add noise to the signal and cause signal deformation, it is important to maintain the insertion loss of a filter as low as possible, meeting the design requirements. Two common methods to reduce the insertion loss are presented in the following two subsections.

2.4.1 Polishing

One method to reduce the losses and increase Q_0 of a resonant cavity is surface polishing. It is done to reduce the imperfections of the conducting surface, commonly named surface roughness. Many surface roughness models have been proposed, which can be divided into two classes. The phenomenological models use formulae or correction factors in order to match the theoretical values to the observed values. The topological models, on the other hand, propose various structures on the conductor surface and analyze their influence using 3-D field simulation. Gold and Helmreich proposed a simple single-parameter model for incorporating surface rougness in the electrical conductivity [12]. To do so, they proposed a location dependent $\sigma(x)$, which varies proportionally to the cumulative distribution function (CDF) of the probability density function (PDF) of surface roughness as

$$\sigma(x) = \sigma_{bulk} \cdot CDF(x) = \sigma_{bulk} \frac{1}{R_{rms}\sqrt{2\pi}} \int_{-\infty}^{x} e^{-\frac{u^2}{2R_{rms}^2}} \,\mathrm{d}u, \tag{2.45}$$

where R_{rms} is the root-mean-squared value of the surface roughness, which has to be measured for the material at hand.

In 2014, the two authors suggested a frequency dependent effective electrical conductivity, $\sigma_{eff}(f)$ [13]. This concept is very practical and allows for simulations with a changed effective conductivity, thus providing results without any additional complexity and required additional computation time. The effective conductivity was measured using a resonant cavity with interchangeable lids with different roughness, while treating the rough surfaces as ideally smooth. For a cylindrical waveguide resonant cavity, as an example, the effective conductivity for a TE mode of resonance can then be calculated from the unloaded Q-factor equation given in Equation (2.7), expressing σ_{eff} from the equation as

$$\sigma_{eff} = \frac{Q_c^2}{\lambda_0^2 f \mu_0} \frac{4\pi\left[\left(p'_{nm}\right)^2 + \frac{2a}{d}\left(\frac{l\pi a}{d}\right)^2 + \left(1-\frac{2a}{d}\right)\left(\frac{nl\pi a}{p'_{nm}d}\right)^2\right]^2}{\left[1-\left(\frac{n}{p'_{nm}}\right)^2\right]^2\left[\left(p'_{nm}\right)^2 + \left(\frac{l\pi a}{d}\right)^2\right]^3}. \tag{2.46}$$

2.4.2 Silver-Plating

Another method, used to minimize losses and, with it, increase the unloaded Q-factor is covering the conductive walls with a sufficiently thick layer of a material with higher conductivity. Specifically, the material with the highest electrical conductivity (at room temperatures) is silver, and the process is called silver-plating. In Table 2.2, the values for electrical conductivity of both the aluminum alloy and silver are provided. The aluminum alloy conductivity is not precisely known, instead a range is given. The electrical conductivity of silver is extracted from CST Microwave Studio [2]. From Equation (2.7) it

material	**electrical conductivity (σ)**
AlMgSi0,5	from $28 \cdot 10^6$ to $35 \cdot 10^6$ S/m
Silver (Ag)	$63.012 \cdot 10^6$ S/m

Table 2.2: Electrical conductivity of AlMgSi0,5 and Ag

can be seen that the imperfectly conducting walls contribution of Q_0 is inversely proportional to the skin depth, which is inversely proportional to the square root of the electrical conductivity, i.e.

$$Q_c \propto \frac{1}{\delta_s} \propto \sqrt{\sigma}. \tag{2.47}$$

By comparing the conductivities of both materials, the following conclusion can be drawn:

$$\frac{Q_{c,Ag}}{Q_{c,alloy}} = \frac{\sqrt{\sigma_{Ag}}}{\sqrt{\sigma_{alloy}}} \implies Q_{c,Ag} \approx (1.34 - 1.5) \cdot Q_{c,alloy}, \tag{2.48}$$

meaning that Q_c should increase somewhere between 34% and 50%, if the surfaces of an aluminum alloy cavity are silver-plated. It is worth noting that this condition is only valid when the thickness of the silver layer is larger than or equal to the skin depth, so that all the electrical current density is confined to that layer.

2.5 Coupling Matrix Based Filter Synthesis

All the necessary concepts, required to build an RF filter, were introduced in the previous sections. A filter is a two-port network, built from a combination of multiple resonators, where some or all are coupled. The goal of a filter is transmitting signals in specified frequency bands and attenuating signals in all other frequency bands. This has to be done with minimized distortion and loss of energy of the transmitted signal. Any realistic physical system has to conform to the causality condition, since it cannot anticipate the future states of its input signal [1, Ch. 3].

2.5.1 Characteristic Polynomials of Lowpass Prototype Filter Networks

The synthesis of a filter starts with the derivation of characteristic polynomials that build the desired reflection and transfer parameters of the filter, which is at this point considered to be a lossless linear two-port network. The reflection coefficient ρ of a two-port network is expressed from the input impedance as

$$\rho(s) = \frac{z_{in}(s) - 1}{z_{in}(s) + 1}, \qquad \text{where } z_{in}(s) = \frac{Z_{in}(s)}{Z_0}. \tag{2.49}$$

Z_0, in this case, is the characteristic impedance of the transmission line and $s = j\omega$ the complex frequency variable. The input impedance is a positive real function, which can be expressed as a quotient of two polynomials, the numerator n(s) and denominator d(s). The reflection coefficient is then expressed as

$$\rho(s) = \frac{n(s) - d(s)}{n(s) + d(s)} = \frac{F(s)}{E(s)}. \tag{2.50}$$

The magnitude of the reflection coefficient is

$$|\rho(j\omega)|^2 = \frac{F(s)F(s)^*}{E(s)E(s)^*} = \frac{F(s)F(-s)}{E(s)E(-s)}. \tag{2.51}$$

In the case of a lossless two-port network, the total power equals the sum of the reflected and transmitted power. The transmission coefficient t follows

$$|t(j\omega)|^2 = 1 - |\rho(j\omega)|^2 = \frac{E(s)E(-s) - F(s)F(-s)}{E(s)E(-s)} = \frac{P(s)P(-s)}{E(s)E(-s)}, \tag{2.52}$$

where the right-hand side of the equation is valid because the root pattern has a quadrantal symmetry and the roots on the imaginary axis have even mutliplicity [1, Ch. 3]. The three polynomials, F(s), P(s), and E(s), are referred to as the characteristic polynomials. Their properties are:

- F(s) is a polynomial with real coefficients, its roots are either real and/or conjugate complex roots. It can have multiple roots only at the origin. The roots represent the frequencies where no power is reflected, called the reflection zeros, and the filter loss is zero.
- P(s) is a pure even polynomial with real coefficients. Its roots lie on the imaginary axis as conjugate pairs and they represent the frequencies at which no power is transmitted, and the filter loss is infinite. The root frequencies are called transmission zeros or attenuation poles. Its roots can also occur as conjugate pairs on the real axis or as a complex quad in the s plane, which leads to linear (nonminimum) phase filters.
- E(s) is a Hurwitz polynomial with real coefficients, with all its roots lying inside the left half of the s-plane.

In the terms of scattering parameters, the transmission and reflection coefficient are more commonly referred to as S_{21} and S_{11}. The two are expressed in terms of the characteristic polynomials as

$$S_{21}(s) = t(s) = \frac{P(s)}{E(s)}, \qquad \text{and} \qquad S_{11}(s) = \rho(s) = \frac{F(s)}{E(s)}. \tag{2.53}$$

Dissipation Factor δ

To include the effect of finite conductivity of the materials, the characteristic functions require an adaptation. This is done by changing the complex frequency variable s to $s+\delta$, where δ is the dissipation factor. The complex frequency variable for the k-th pole or zero is then $s = s_k - \delta$. In terms of a lowpass prototype, δ is inversely proportional to Q_0 of the resonator. In bandpass filters, the frequency transformation from lowass to bandpass has to be considered, which is

$$\omega' = \frac{\omega_0}{\Delta\omega}\left(\frac{\omega}{\omega_0} - \frac{\omega_0}{\omega}\right). \tag{2.54}$$

The dissipation factor δ of a bandpass filter is then derived to be

$$\delta = \frac{\omega_0}{\Delta\omega}\frac{1}{Q_0}. \tag{2.55}$$

FIR Elements

It is sometimes required, that the filter has an asymmetric response in either amplitude, phase, or both. For example, when very high signal suppresion in a certain frequency range is required, a transmission zero can be used. In bandpass prototype networks, this is possible, however the lowpass prototype filters always result in a symmetric response with regards to zero. A frequency transformation from a symmetric lowpass circuit to a passband circuit always leads to a symmetric passband circuit. To be able to create a lowpass prototype network which would transform into the appropriate asymmetric filter response, frequency-invariant response (FIR) elements were introduced. They are hypothetical elements which only become realizable after the frequency transformation.

Generation of Transfer and Reflection Polynomials

The generation of transfer and reflection polynomials for an arbitrary frequency response is generally a complex procedure, requiring computer-aided optimization procedures. For some more common types of filters, however, analytical models for determining the critical frequencies exist. The most common among them are the maximally flat Butterworth filters and the equiripple Chebyshev filters. Due to the asymmetric response of the filter that is to be designed in the course of this thesis, a more complex filter response is needed. Thus, CST Filter Designer 3D (FD3D) is used for the derivation of the coupling matrix and the methods to construct transfer and reflection polynomials will be omitted at this point.

2.5.2 Coupling Matrices

A filter network can be represented by a matrix consisting of the self-resonances of the filter's individual resonators and the couplings between them. The matrix form of the circuit allows for common matrix operations, such as inversion, similarity transformation, and partitioning. With help of these operations, the synthesis and topology reconfiguration are substantially simplified. Each element in the matrix represents a realistic element in the finished device. A general lowpass prototype circuit model for a filter with an asymmetric response with all possible couplings is shown in Figure 2.6. The coupling elements, labeled with $\mathrm{M}_{k,l}$, are assumed frequency-invariant, and FIR elements allow the circuit to represent asymmetric characteristics, as discussed in the previous section. The

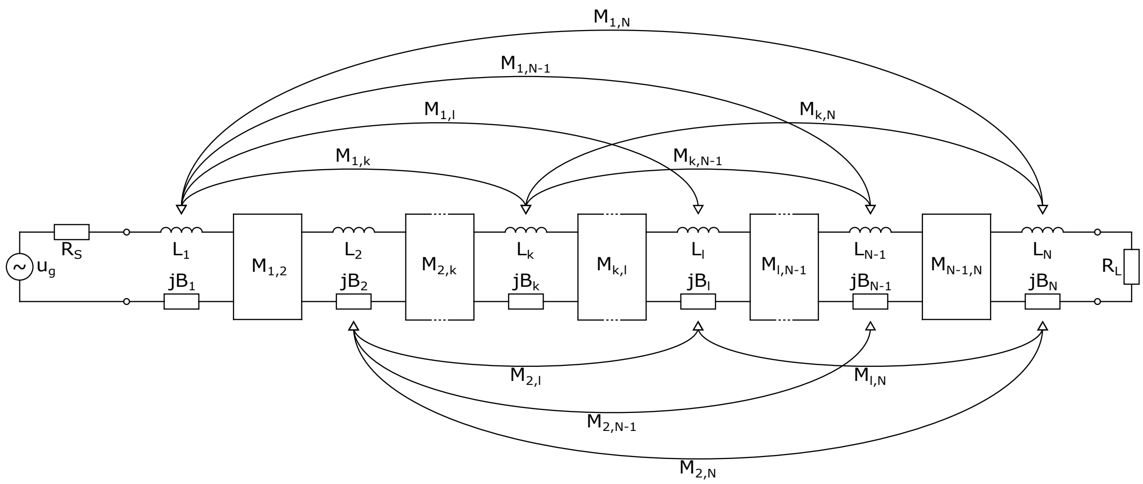

Figure 2.6: General asymmetric lowpass filter prototype circuit

impedance matrix of the two-port network in Figure 2.6, comprising of a sum of three contributions, is

$$\mathbf{Z} = [j\mathbf{M} + s\mathbf{I} + \mathbf{R}], \tag{2.56}$$

where $\mathbf{M}$ is the main coupling matrix, j the imaginary unit, $\mathbf{I}$ the unit matrix, $s = j\omega$ the complex frequency variable and $\mathbf{R}$ the termination impedance matrix [1, Ch. 8]. The dimension of all three matrices is N·N. The values of mainline couplings between the sequentially numbered nodes $M_{k,k+1}$, self-couplings on the main diagonal $M_{k,k}$, represented by the FIR elements B_k, and cross-couplings between non-sequential nodes, $M_{k,l\neq(k\pm1)}$ build the first matrix as

$$\mathbf{M} = \begin{bmatrix} M_{1,1} & M_{1,2} & M_{1,3} & \dots & M_{1,N} \\ M_{2,1} & M_{2,2} & M_{2,3} & \dots & M_{2,N} \\ \vdots & \vdots & \vdots & \ddots & \vdots \\ M_{N,1} & M_{N,2} & M_{N,3} & \dots & M_{N,N} \end{bmatrix} = \begin{bmatrix} B_1 & M_{1,2} & M_{1,3} & \dots & M_{1,N} \\ M_{1,2} & B_2 & M_{2,3} & \dots & M_{2,N} \\ \vdots & \vdots & \vdots & \ddots & \vdots \\ M_{1,N} & M_{2,N} & M_{3,N} & \dots & B_N \end{bmatrix}, \tag{2.57}$$

where due to the symmetry of the couplings, the matrix is symmetrical over the main diagonal. The second matrix, I, contains the frequency variable portion on the main diagonal, $s = j\omega$, and the third matrix, R, contains the source impedance at $\mathrm{R}_{1,1} = R_S$ and load impedance at $\mathrm{R}_{\mathrm{N,N}} = R_L$.

N+2 Coupling Matrix

By inserting impedance inverters $M_{S,1}$ and $M_{N,L}$ of values $\sqrt{R_{1,1}}$ and $\sqrt{R_{N,N}}$ into the circuit in Figure 2.6, the (nonzero!) source and load terminantions can be normalized. The total transformed admittance circuit is presented in Figure 2.7. It can be seen that

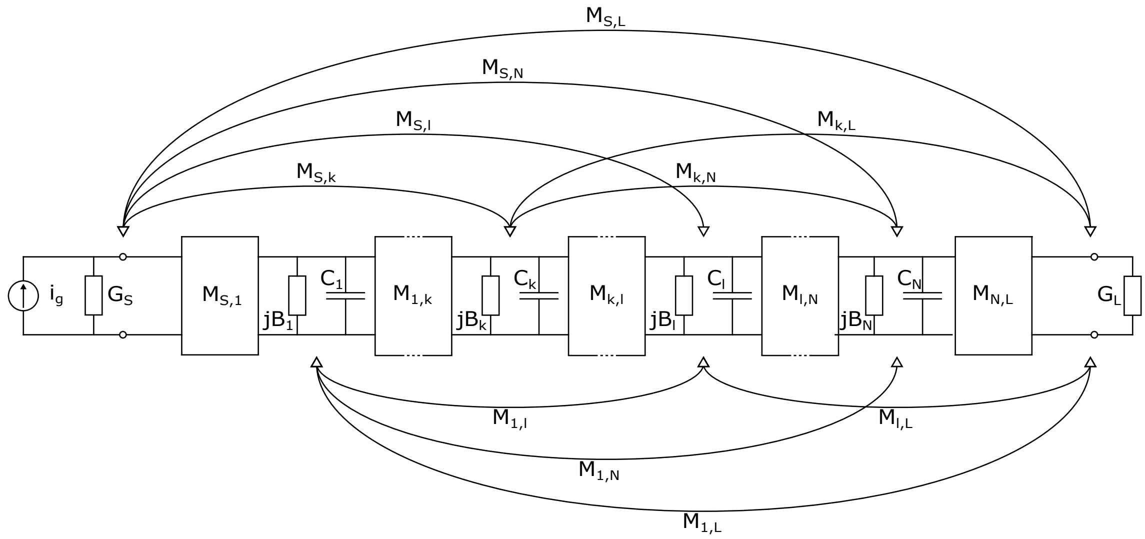

Figure 2.7: N+2 lowpass filter prototype with parallel resonators

additional coupling from source/load to nodes other than the first/last and direct coupling between source and load are now included. The full (N+2)·(N+2) coupling matrix, commonly called N+2 matrix, can then be written as

$$\mathbf{M} = \begin{bmatrix} M_{S,S} & M_{S,1} & M_{S,2} & \dots & M_{S,N} & M_{S,L} \\ M_{S,1} & M_{1,1} & M_{1,2} & \dots & M_{1,N} & M_{1,L} \\ M_{S,2} & M_{1,2} & M_{2,2} & \dots & M_{2,N} & M_{2,L} \\ \vdots & \vdots & \vdots & \ddots & \vdots & \vdots \\ M_{S,L} & M_{1,L} & M_{2,L} & \dots & M_{N,L} & M_{L,L} \end{bmatrix}. \tag{2.58}$$

A coupling matrix can be synthesized from the lowpass prototype circuit, designed beforehands, or directly from the S-parameter polynomials. The direct method will be discussed here. It can be done both for the N·N matrix and for the N+2 matrix. Both cases follow the same approach, that is to formulate the admittance parameters in two ways: first from the filter polynomials F(s), P(s), and E(s), which make up the desired S-parameter characteristics, and second from the coupling matrix itself. The two formulations are then equated to relate the coupling values to the coefficients of the S-parameter polynomials.

2.5.3 Coupling Matrix Reduction

The coupling matrix, derived in the previous section, has all the resonators directly coupled to the input and/or output. Realization of such a structure is highly unpractical, therefore coupling matrix reduction has to be done. A sequence of similarity transformations, also called rotations, is done, minimizing the number of couplings. A similarity transformation is done by pre- and postmultiplying the coupling matrix $\mathbf{M}$ with a rotation matrix $\mathbf{S}$ and its transpose $\mathbf{S}'$ as

$$\mathbf{M_T} = \mathbf{S} \cdot \mathbf{M} \cdot \mathbf{S}'. \tag{2.59}$$

A rotation matrix for a pivot {k,l} ($k \neq l$) consists of elements $S_{k,k} = R_{l,l} = cos(\Theta_r)$, $R_{l,k} = -R_{k,l} = sin(\Theta_r)$, where Θ_r is the rotation angle. Other elements on the main diagonal are one, and the remaining elements are zero. The similarity transformation only affects the k-th and l-th rows and columns and furthermore, if elements, facing each other across the rows and columns of the pivot of a transformation, are zero before the transformation, they remain zero after it. Due to these two properties, the similarity transformation is useful for coupling matrix reduction. [1, Ch. 8] gives the rotation angle Θ_r formulas for annihilating specific elements in the coupling matrix with a rotation at pivot {k,l} as

$$\begin{aligned}
&\Theta_r = tan^{-1}(M_{k,m}/M_{l,m}), \quad \text{for the m-th element in row k } (M_{k,m})\\
&\Theta_r = -tan^{-1}(M_{l,m}/M_{k,m}), \quad \text{for the m-th element in row l } (M_{l,m})\\
&\Theta_r = tan^{-1}(M_{m,k}/M_{m,l}), \quad \text{for the m-th element in column k } (M_{m,k})\\
&\Theta_r = -tan^{-1}(M_{m,l}/M_{m,k}), \quad \text{for the m-th element in column l } (M_{m,l})\\
&\Theta_r = tan^{-1}\left(\frac{-M_{k,l} \pm \sqrt{M_{k,l}^2 - M_{k,k}M_{l,l}}}{M_{l,l}}\right), \quad \text{for cross-pivot element } (M_{k,k})\\
&\Theta_r = tan^{-1}\left(\frac{M_{k,l} \pm \sqrt{M_{k,l}^2 - M_{k,k}M_{l,l}}}{M_{k,k}}\right), \quad \text{for cross-pivot element } (M_{l,l})\\
&\Theta_r = \frac{1}{2}tan^{-1}\left(\frac{2M_{k,l}}{M_{l,l} - M_{k,k}}\right), \quad \text{for cross-pivot element } (M_{k,l})
\end{aligned} \tag{2.60}$$

Which elements are selected to be nonzero and which not depends on the design. Numerous realizations exist, the next section will focus on the realization selected for our filter.

2.5.4 Box Section Filters

As stated earlier, if a filter requires high signal suppression in a certain frequency range, it can be designed with an asymmetric response with regards to its center frequency. This is realized by implementing a transmission zero in the stopband. In the sense of filter configurations, the minimum structure capable of realizing such a transmission zero is a trisection. It consists of three mutually coupled nodes and is able to realize one transmission zero. Depending on the position of the transmission zero, the cross-coupling is positive or negative. In the case of a transmission zero below bandpass, a negative cross-coupling is required, while a positive cross-coupling is needed for a transmission zero above bandpass. The realization of the two couplings will be discussed further in Section 2.6. Trisections can be joined together to build larger, more complex structures. The cross coupling in each trisection of the joint structure still describes its particular transmission zero. The inherent limitation of a trisection, when talking about filter manufacturing, is its requirement for a diagonal coupling. These are typically difficult to manufacture.

In order to simplify the structure and avoid diagonal couplings, box section configuration can be used [1, Ch. 10]. The formation of a box section from a trisection is presented in

Figure 2.8. A cross-pivot similarity transformation is done on the trisection, seen left in the figure. The transformation annihilates the coupling between the resonator pair {2,3} and instead couples the resonator pair {2,4}, which can be seen in the middle setup in the figure. By untwisting, that is switching the location of resonator 3 and 4, the box section is created, seen in the figure on the right side. It can be seen that the diagonal coupling

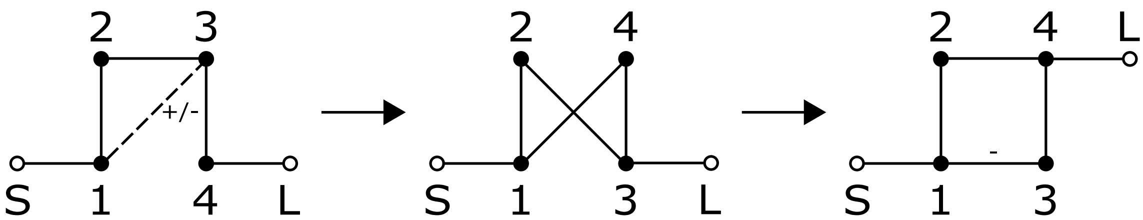

Figure 2.8: The formation of the box section configuration

in the setup has been eliminated and the coupling between resonator pair {1,3} is now negative. From the setup, the coupling matrix is given as

$$\mathbf{M} = \begin{bmatrix} 0 & M_{S,1} & 0 & 0 & 0 & 0 \\ M_{S,1} & M_{1,1} & M_{1,2} & M_{1,3} & 0 & 0 \\ 0 & M_{1,2} & M_{2,2} & 0 & M_{2,4} & 0 \\ 0 & M_{1,3} & 0 & M_{3,3} & M_{3,4} & 0 \\ 0 & 0 & M_{2,4} & M_{3,4} & M_{4,4} & M_{4,L} \\ 0 & 0 & 0 & 0 & M_{4,L} & 0 \end{bmatrix}. \quad (2.61)$$

This coupling matrix represents the final structure, which can be used for realizing the bandpass filter at hand.

2.6 Realization of Physical Structures

A synthesized coupling matrix of a filter provides all the normalized mathematical coupling values, which correspond to a specific behavior of a filter. It does not, however, provide any physical models. To manufacture a filter, the translation of matrix values to physical elements is needed. This section will provide the necessary steps to derive actual filter structures, which realize the resonances and the couplings described in the coupling matrix. Before talking about designing the structures, some important filter parameters have to be presented. The center frequency of a filter is defined as

$$f_0 = \sqrt{f_U \cdot f_L}, \quad (2.62)$$

where f_U and f_L are the upper and lower band edges of the filter passband bandwidth, as given in the specifications. The bandwidth of a filter, BW, is defined as the difference between f_U and f_L, as

$$\mathrm{BW} = f_U - f_L. \quad (2.63)$$

The fractional bandwidth, FBW, is then

$$\mathrm{FBW} = \frac{\mathrm{BW}}{f_0}. \quad (2.64)$$

The physical realization procedure will be introduced on an example of coaxial quarter-wavelength resonators, which will also be used for the design and production of the filter, as discussed in more detail in Section 3.2. In [14], Hagensen describes the design of such a filter. To avoid a design of the ideal structure, which perfectly fits the desired operation, tunability of the filter parameters is required in practice. This is done with tuning screws. The construction of tunable physical structures, corresponding to coupling matrix parameters, will be discussed in the following subsections. The relations between the coupling matrix coefficients and values which can be measured and/or simulated are given in the CST Online Help [2].

2.6.1 Individual Resonator

The elements on the main diagonal of the coupling matrix are realized with resonators, which are offset from the center frequency, if the value of the element is nonzero. The general expression to determine the self-resonant frequency of a resonator from its coupling matrix value is

$$f_{res,k} = f_0 \left(\sqrt{1 + \left(-m_{k,k} \frac{\mathrm{FBW}}{2} \right)^2} + m_{k,k} \frac{\mathrm{FBW}}{2} \right). \tag{2.65}$$

For simplicity, all resonators can be designed with the same dimensions. The frequency offset is then realized with a tuning screw, which is sunk in the center of the inner conductor. The resonant frequency decreases with tuning screw length, thus the initial resonator is designed for a higher frequency, i.e. a shortening factor n is suggested for the length of the resonator. As a rule of thumb, Hagensen proposes a shortening factor $0.5 \leq n \leq 0.8$ [14]. An experimental Q_0 equation is proposed,

$$Q_0 = 0.75 \cdot \frac{n\lambda}{\delta} \frac{1}{4 + \frac{n\lambda}{a} \cdot \frac{1+a/b}{ln(a/b)}}, \tag{2.66}$$

where the factor of 0.75 is suggested as an estimate of the additional losses due to the lower realistic surface conductivity, surface roughness and the influence of the tuning screws. In the case that the shape of the cavity is not circular, Hagensen suggests that the equivalent circular diameter is determined from the base area of the structure.

2.6.2 External Coupling

The external coupling is usually given in the form of an external quality factor. The factor is obtained from the coupling matrix by using the normalized coupling coefficient as

$$Q_{ext} = \frac{1}{(m_{S/L,i})^2 \cdot \mathrm{FBW}}. \tag{2.67}$$

Different mechanisms for coupling of the energy to the resonator exist. When connecting 3-D filters to coaxial transmission lines, the most common options are either a coupling probe or a coupling loop. A coupling probe is a length of the connector inside the resonant structure, which is left unconnected. This induces a strong coupling of the electric field, i.e. the coupling is capacitive. The other option, the coupling loop, is a connector wire connected to the surface of the cavity, forming a loop. This induces a strong magnetic field coupling, and is thus called inductive coupling. The coupling loop mechanism is shown in Figure 2.9. To determine the amount of external coupling, simulations of the coupling mechanism are required.

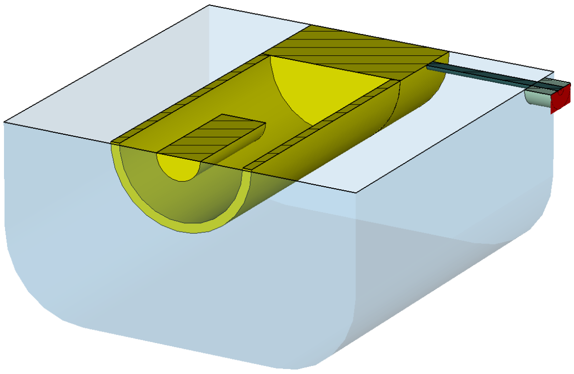

Figure 2.9: Symmetry plane cross-sectional view of a single resonator with a coupling loop mechanism between the inner and the outer conductor

2.6.3 Interresonator Coupling

The interresonator coupling coefficient from Equation (2.14) can be obtained from the coupling matrix as

$$\kappa_{k,l} = m_{k,l} \cdot \mathrm{FBW}, \tag{2.68}$$

The sign of the coupling coefficient determines the type of coupling mechanism, either inductive or capacitive. The coupling is commonly expressed in the terms of a coupling bandwidth CBW as

$$\mathrm{CBW} = m_{k,l} \cdot \mathrm{BW}, \tag{2.69}$$

Inductive Coupling

The positive coupling matrix coefficients, which are not on the main diagonal of the coupling matrix, represent an inductive coupling mechanism between the corresponding resonator pairs. Different mechanisms for realization of such a coupling exist. The most simple approach is using an iris opening in the filter wall between the two resonators, as presented in Figure 2.10. Another method suggests constructing a loop in the opening in the wall between the resonator pair [15]. The advantage of the iris realization is that tuning screws can be used, which affect the amount of coupling, and is therefore favored. The computation of the amount of coupling between 3-D resonant structures is a complex mathematical process, which requires the simulation of the electric and magnetic fields, as presented in Section 2.2. The coupling values are obtained from simulation results.

Capacitive Coupling

The negative coupling matrix coefficients, which are not on the main diagonal of the coupling matrix, represent a capacitive coupling mechanism between the corresponding

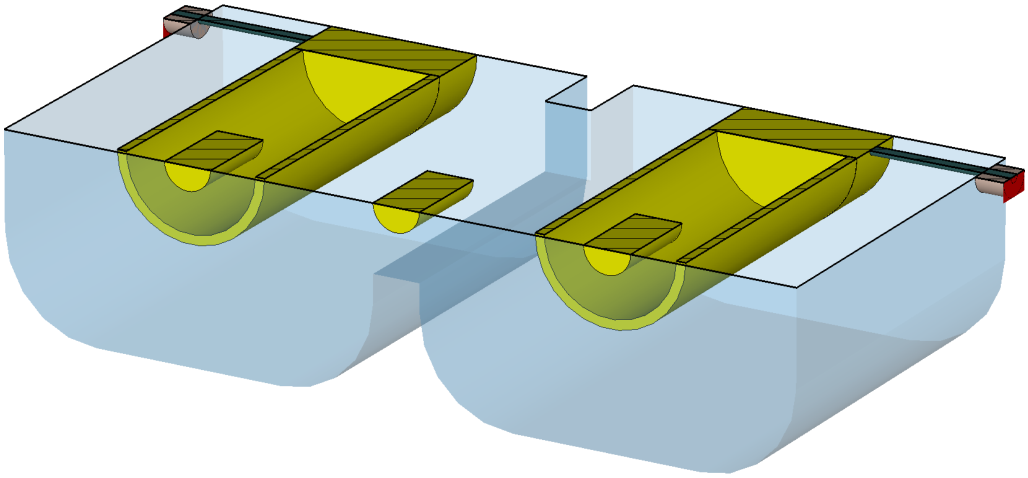

Figure 2.10: Symmetry plane cross-sectional view of the inductive coupling iris mechanism

resonator pairs. The most typical realization of a capacitive coupling is a conductive probe, placed in the filter wall between the resonators [15]. An example is shown in Figure 2.11. As in the case of any other coupling mechanism, analytical solution is difficult to obtain

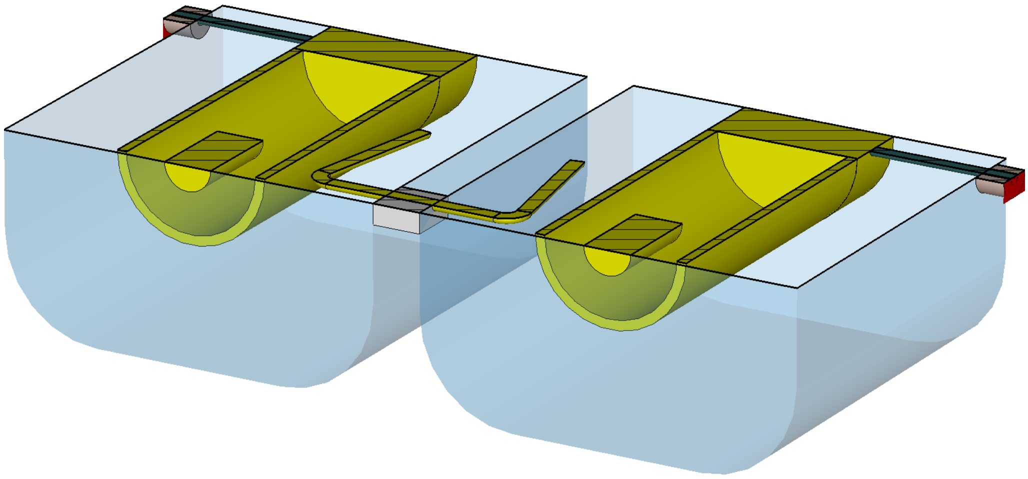

Figure 2.11: Symmetry plane cross-sectional view of the capacitive coupling probe mechanism

and simulation tools are used to get the coupling bandwidth.

3 Design Process

The aim of the chapter at hand is to provide the reader with a detailed step-by-step description of the design process. It is structured into two separate sections, one for the single resonant cavity and the other one for the BPF, both having three subsections. The first of the subsections discusses the synthesis and calculations required for the design, the second subsection discusses the simulations required, while the last subsection talks about the actual manufacturing of the designed devices.

Section 3.1 focuses on the resonant cavity. In the calculus subsection, the resonant frequencies of the lowest six modes are calculated based on the cavity dimensions. The process is continued in the simulations subsection, where the propagation mode field distributions can be observed using 3-D EM simulations. The coupling of energy to the cavity can be simulated in order to optimize the coupling. Effects of changing the electrical conductivity or surface roughness of the conducting walls can also be simulated. The last subsection presents the actual production procedure and the procedures used to improve the surface of the conducting walls. In Section 3.2, the bandpass filter design process is discussed. As stated above, the topic is divided into three major subsections, starting with the matrix synthesis process, from which the coupling coefficients are obtained. The initial filter structure dimensions are also calculated here, giving the physical dimensions of the filter. These values are then used to proceed to the next subsection, where the filter is modeled in a simulation environment and the calculated parameters adapted accordingly. The simulation part of the process leads us to a full filter model, ready to be produced. This part of the process is discussed in the final subsection, devoted to shed light on the manufacturing of the BPF.

3.1 Resonant Cavity

To minimize all the imperfections, caused by the production of a resonant cavity, a simple cylindrical cavity was to be designed. The goal was to simply dive the milling cutter into the aluminum alloy solid to obtain the resonant cavity. A milling cutter with a diameter of 22 mm and a height of 40 mm was selected, thus providing both the cylindrical cavity dimensions.

3.1.1 Calculations

Following Equations (2.3) and (2.4), using the milling cutter parameters, the first six modes and their frequencies of resonance were found, listed in Table 3.1. The mode with the lowest frequency, TE_{111}, was selected for further calculations and was used for the final measurements of Q_0. Then, the theoretical values for Q_0 could be calculated

mode	resonant freq.
TE_{111}	8821.066 MHz
TM_{010}	10 431.896 MHz
TE_{112}	10 951.729 MHz
TM_{011}	11 084.561 MHz
TM_{012}	12 845.102 MHz
TE_{211}	13 766.836 MHz

Table 3.1: The first 6 resonant modes with their corresponding resonant frequency

from Equation (2.5). Since the cavity is not filled with a dielectric, Q_0 was obtained by calculating the contribution of the imperfectly conducting walls in Equation (2.7). This was done for both the aluminum alloy cavity and the silver-plated cavity, which is covered with a sufficiently thick layer of silver. Sufficiently thick in this context means larger than the skin depth δ_S, so that the current density is restricted to the silver layer. The results are shown in Table 3.2, where a range of unloaded Q-factors is given for the aluminum alloy corresponding to its range of probable electrical conductivity.

material	$Q_{0,\mathbf{theoretical}}$
AlMgSi0,5	8122-9081
silver	12 185

Table 3.2: Theoretical results for Q_0 of TE_{111} mode

3.1.2 Simulations

The simulations were done in two steps, one to obtain the resonant modes and the other to get the S-parameters of the complete structure. For the simulations, CST Microwave Studio was used.

Resonant Modes

To obtain all the resonant modes in the selected frequency range and their field distributions, a trivial vacuum cylinder was modeled. A frequency range from 0 to 18 GHz was used, since the selected SMA connectors typically operate in this frequency range. Due to the fast convergence, eigenmode solver with tetrahedral meshing was used for the simulation of resonant modes, which does not consider losses in the solution. Therefore, the background, that is the surrounding material of the vacuum cavity model, was set to perfect electric conductor (PEC) in this step and boundary conditions were set to $E_t = 0$. The solver calculates the frequencies and the corresponding field patterns (eigenmodes), while no excitation needs to be applied. Although real materials are not considered in the simulation, an additional post-processing step gives the Q_0 calculation based on the given conductivity. In Tables 3.3 and 3.4, a comparison for the resonant frequencies and Q_0 at TE_{111} is displayed. Due to the symmetry of the cavity, the orthogonal TE modes

mode	**calculated freq.**	**simulated freq.**	$\lvert \Delta f \rvert$
TE_{111}	8821.066 MHz	8821.789 MHz	723 kHz
TM_{010}	10 431.896 MHz	10 431.140 MHz	756 kHz
TE_{112}	10 951.729 MHz	10 952.313 MHz	584 kHz
TM_{011}	11 084.561 MHz	11 083.851 MHz	710 kHz
TM_{012}	12 845.102 MHz	12 844.490 MHz	612 kHz
TE_{211}	13 766.836 MHz	13 767.830 MHz	994 kHz

Table 3.3: Calculated vs. simulated resonant frequencies

should have the same resonant frequency, but the simulation gives slightly different results. Since the difference is smaller than a kilohertz, it is smaller than the rounding error of the results. Thus, the difference can be neglected. It can be seen, that the variations between

material	**calculated Q_0**	**simulated Q_0**	$\lvert \Delta Q_0 \rvert$
AlMgSi0,5	8122 - 9081	8110 - 9068	12 - 13
silver	12 185	12 167	18

Table 3.4: Calculated vs. simulated Q_0 for TE_{111}

the calculated and simulated results are very small. Specifically, the variation of simulated results from the calculated results is found to be less then 1500 ppm. The difference is mainly caused by rounding errors in both the calculations and simulations, and in the limited numerical simulation resources, which result in an offset from the analytical model. If required, reducing the mesh size of the simulation model would reduce the variations even further.

Reflection Parameters

Next, the goal was to model a more realistic physical device, with a mechanism to couple energy to the resonant cavity. An SMA connector was modeled and a waveguide port defined on it, which applies an EM field at the port reference plane. The complete model is portrayed in Figure 3.1. The teflon of the connector was assumed to be cut to the cavity edge. The connector was placed in the middle of the cavity height, which supports coupling to the TE_{111} mode. The length of the connector pin is the variable which was varied to change the coupling coefficient. The background was now set to a lossy metal with a realistic conductivity, either aluminum alloy or silver. The boundary conditions were changed from the previous idealistic setup to conducting walls, which accept the electrical conductivity as the only parameter. Taking into account the defined excitation and the lossy materials used, a different solver was needed. Specifically, the frequency domain solver was used. When compared to the time domain solver, this is the better option due to the long settling time of strongly resonant structures, which make time domain simulation times very long. The results of the solver are the S-parameters for the defined ports. In this case, the S_{11} parameter was obtained. The goal of the simulation

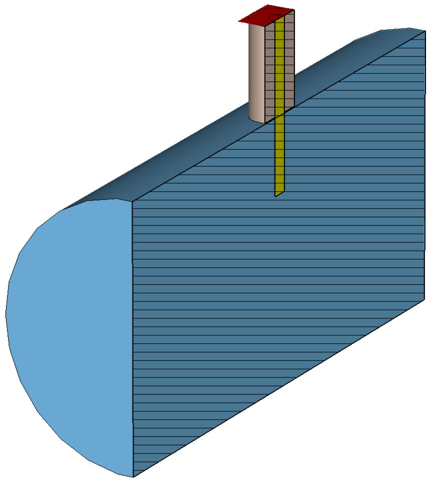

Figure 3.1: Symmetry plane cross-sectional view of the resonant cavity model

was to find three different pin lengths, one for coupling close to critical (C_1), one for an overcritical coupling (C_2), and one for an undercritical coupling (C_3), as described in Section 2.2. Multiple connectors were used in order to observe the variations of the Q-factor estimation. Ideally, the goal is to obtain a constant result, since the real Q-factor is independent of the coupling mechanism. The simulated Q-circles for the selected three pin lengths are shown in Figure 3.2.

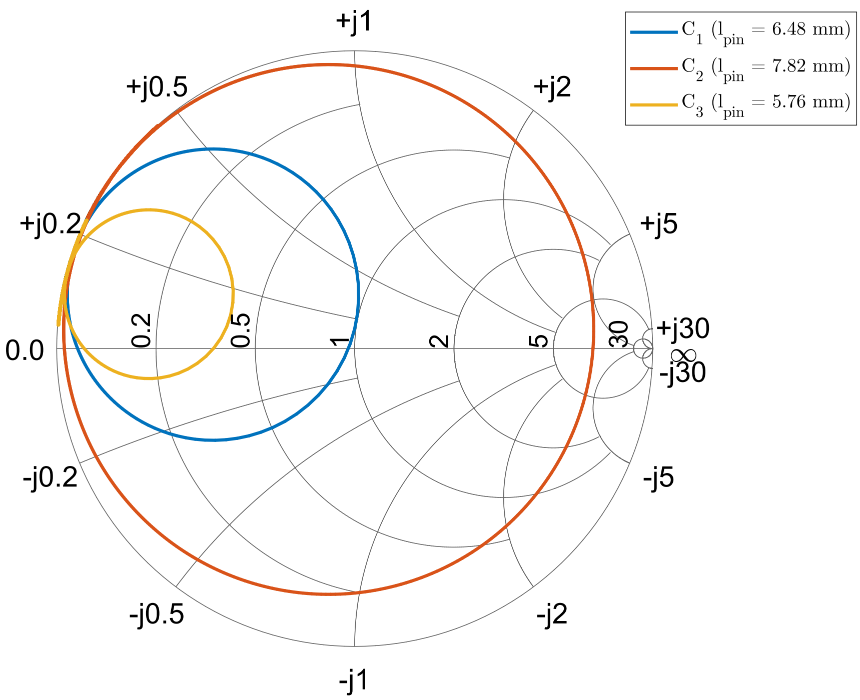

Figure 3.2: Q-circle simulations for the three selected pin lengths

3.1.3 Production

Knowing the desired dimensions of the cavity and the connector probe lengths, the cavity and the connectors could now be constructed. The one parameter that has not been discussed yet is the wall thickness of the resonator. The thickness should be large enough to drill holes for the screws of the covers and mount the connector. It was found that a thickness of 6 mm is a good option. This thickness is also much larger than the skin depth at the frequencies of interest, so the cavity is electromagnetically sealed. The connectors were chosen in accordance with the simulation results (C_1 = 6.42 mm, C_2 = 7.82 mm, and C_3 = 5.76 mm) and can be seen in Figure 3.3. Two test cavity samples

Figure 3.3: Connectors: C_1 (left), C_2 (middle), and C_3 (right)

were originally built, one to be polished and the other to be silver-plated. One was made with the aforementioned milling cutter with a diameter of 22 mm. Initially, the cutter was supposed to be dived in a piece of aluminum with a height larger than 40 mm so that a cover would be required on one side only. When testing this method, the bottom of the cavity was found to be very rough. The model was then modified to cut through a 40 mm high piece of aluminum, closing it with a cover on both sides. The first cavity was built following this procedure, and the 22 mm cutter was found to vibrate significantly, causing scratch marks on the surfaces. The second cavity was built by firstly diving a less vibrating smaller milling cutter and later cutting the edges until the desired diameter of 22 mm was reached. The difference between the cavities can be observed in Figure 3.4.

Figure 3.4: Comparison: cavity 1 (left) vs. cavity 2 (right)

Surface Processing

After measuring the S-parameters of the manufactured resonant cavities, the cavities were ready for surface processing. Cavity 1, which had a visually rougher surface, as seen in Figure 3.4, was polished using a polishing paste. The difference between the unpolished and polished surface can be seen in Figure 3.5. Cavity 2 was selected for silver-plating.

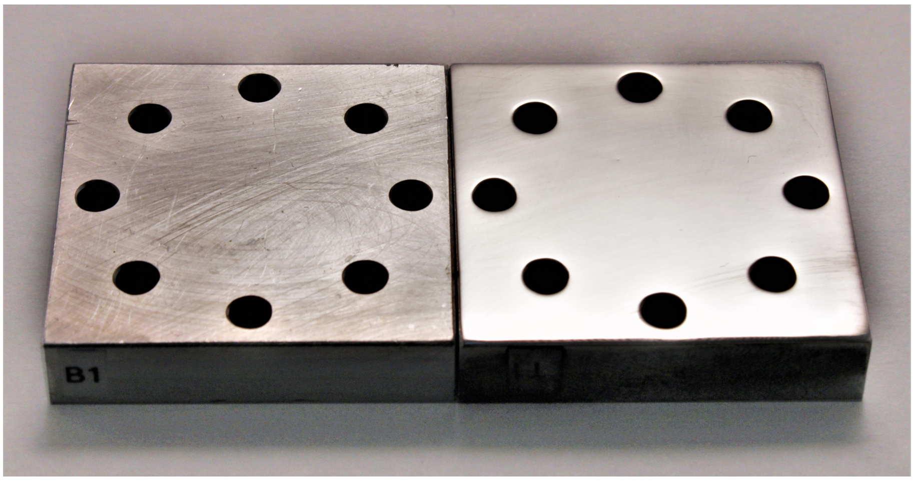

Figure 3.5: Comparison: unpolished cover (left) vs. polished cover (right)

Since the equipment needed to do this is not available in-house, the silver-plating was outsourced to a company that specializes in metal-plating. Unfortunately, the silver-plating process of the company used a less-conductive nickel (Ni) layer under the silver layer, deteriorating the connection between the outer and inner surfaces of the cavity, increasing the amount of losses and decreasing Q_0. This will be discussed in further detail later. At this point, a third cavity had to be built, cavity 3, which was sent to a different company for the silver-plating process. This company used copper as the intermediary layer, allowing for a better plating for the given aluminum alloy. Both silver-plated cavities are shown in Figure 3.6.

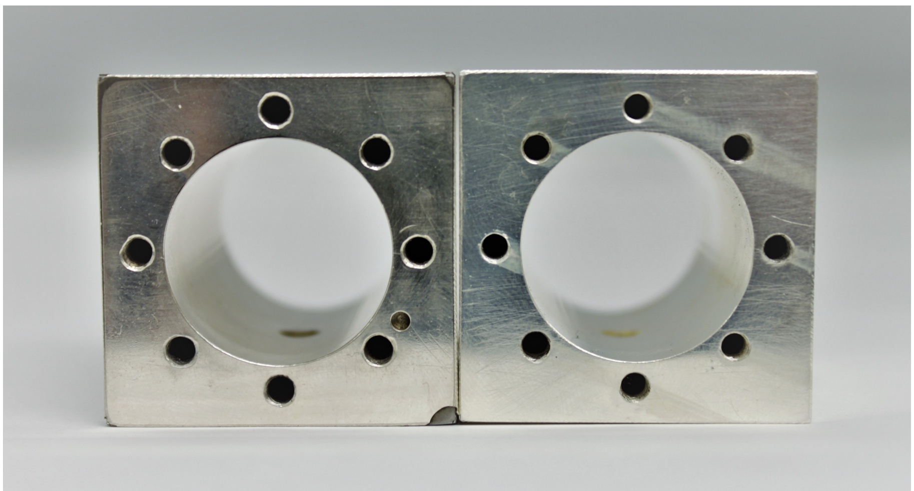

Figure 3.6: Silver-plated cavities: cavity 2 (left) and cavity 3 (right)

3.2 Bandpass Filter

Every filter design process starts from the same point, the desired filter specifications. More specifically, for the passband, the required specifications are the frequency range, the minimum return loss, the maximum insertion loss and/or ripple. For the stopband, the minimum attenuation and the frequency range for this attenuation has to be defined. If a certain frequency band needs to be suppressed in particular, this can also be stated in the specification. The initial specifications for this work are listed in Table 3.5. These will be revisited later, when modifications will have to be made, mainly due to the in-house production, based on the trade-off between the performance and the complexity of the structure. From the specifications in Table 3.5, the upper band-edge frequency f_U and

passband	return loss/ripple	insertion loss	channel suppresion
963.5...970.5 MHz	≤ 1 dB	≥ 20 dB	971.5...978.5 MHz

Table 3.5: Bandpass filter specifications

the lower band-edge frequency f_L are found to be $f_U = 970.5$ MHz and $f_L = 963.5$ MHz. The center frequency, filter bandwidth, and the fractional bandwidth can be calculated from the two edges, using Equations (2.62) to (2.64). The values are listed in Table 3.6.

parameter	value
f_0	967 MHz
BW	7 MHz
FBW	0.00724

Table 3.6: Filter parameters

3.2.1 Synthesis and Calculations

The derivation of the filter functions and the construction of the coupling matrix is generally a demanding procedure. However, software is readily available for the design, which assists the designer with these tasks. To obtain the coupling matrix, CST FD3D was used. The filter specifications were provided to the software and the box section filter with four resonant nodes was selected. The structure was limited to four resonators in order to maintain the structure compact and easy to manufacture. The box section filter was selected to avoid the need for a diagonal coupling when realizing the required transmission zero at 975 MHz, necessary for achieveing good suppression of the neighboring channel. The software then computed the optimal coupling matrix for this given case. The resulting coupling matrix is shown in Table 3.7. The resonant frequencies of the individual resonators were calculated from the coupling matrix elements on the main diagonal, following Equation (2.65), and are listed in Table 3.8. The external coupling bandwidths for source and load are typically represented with external Q-factors, Q_{ext}. Both are the same in our example, $Q_{S,1} = Q_{4,L} = 129.199$, which can also be observed in the equal coupling matrix values in Table 3.7 ($M_{S,1} = M_{4,L} = 1.034$). The couplings between resonators are typically represented by coupling bandwidths. They are listed in Table 3.9. Quarter-wavelength coaxial resonators were selected for the filter due to their small size

	S	**1**	**2**	**3**	**4**	**L**
S	0.000	1.034	0.000	0.000	0.000	0.000
1	1.034	0.039	0.740	-0.528	0.000	0.000
2	0.000	0.740	0.536	0.000	0.740	0.000
3	0.000	-0.528	0.000	-0.845	0.528	0.000
4	0.000	0.000	0.740	0.528	0.039	1.034
L	0.000	0.000	0.000	0.000	1.034	0.000

Table 3.7: Coupling matrix of a box section filter

no.	**frequency**
1	966.857 MHz
2	965.120 MHz
3	969.955 MHz
4	966.857 MHz

Table 3.8: Resonant frequencies obtained from the coupling matrix

when comparing to other 3-D resonators, as discussed in Section 2.1. The resonators were then to be tuned to the exact required frequencies using the tuning screws. As mentioned in Section 2.6, a shortening factor between $n = 0.5$ and $n = 0.8$ should be chosen for the design of the resonator. The value of $n = 0.51$ was found to give the resonator height of

$$h = n \cdot \frac{c_0}{4f_0} \approx 39.5\ mm, \tag{3.1}$$

which is the minimum suggested value, which can be rounded to a precision of 0.5 mm. The shape of the outer resonator wall was selected to be square rather than circular, which is much easier to manufacture with a milling machine. The size of the square resonator was chosen to be 40 mm, again the main reason was to keep the structure compact. Due to the fact that sharp square edges are difficult to manufacture with the available equipment, the edges were rounded instead, with a radius of 9 mm. The calculation of the equivalent circle radius with the same shape area gives

$$S_{shape} = a^2 - (4-\pi)r^2 \Rightarrow r_{eqc} = \sqrt{\frac{a^2 - (4-\pi)r^2}{\pi}} \approx 22.07\ mm. \tag{3.2}$$

M5 tuning screws were selected. Note that the diameter of the tuning screws was chosen only because these screws were readily available with a fine thread, which was important to keep the screws stable in position. Screws with smaller diameter would allow making the inner conductor smaller, thus improving the resonator quality. However, the available screws were preferred, hence, a sub-optimal design was accepted. The inner conductor is hollow, so that the tuning screws can be dived into the center. This allows the minimization of the total cavity height, which then needs to be slightly higher than the inner conductor to realize the open circuit at one side of the coaxial resonator. In literature, the dimensions of the resonators are often based on empirical values, hence the values here are often based on best-guess strategies and are optimized in the simulation process. The gap between the inner conductor and the cavity wall, for example, follows this method. A simulation was done using different gap heights between the inner conductor and the wall of the cavity. It was found, that the frequency decreases significantly when approaching the cavity wall.

pair	bandwidth
1-2	5.182 MHz
1-3	-3.699 MHz
2-4	5.182 MHz
3-4	3.699 MHz

Table 3.9: Inter-resonator coupling bandwidths

A gap of 0.5 mm was identified as the best gap width, that can still be realized, giving the total cavity height of 40 mm. The outer radius of the inner conductor, b, was selected to be 8 mm, which is not the optimum Q-factor size, determined to be $b_{opt} = r_{eqc}/3.6 = 6.13$ mm. This larger radius was selected to avoid short-circuiting the cavity with the tuning screw. One should also bare in mind, that b is the outer radius of a hollow conductor, while the inner radius is smaller for the thickness of the conductor, which was selected to be 1 mm, as this was the minimum safely obtainable thickness with the avaliable machines. The final shape of the cavity and its circular equivalent are shown in Figure 3.7 and the dimensions of the resonators are shown in Figure 3.8. For the inner conductor, brass was

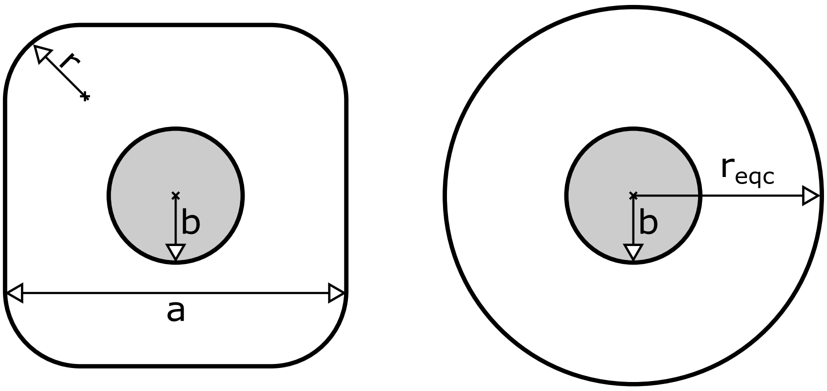

Figure 3.7: Resonator shape vs. circle with equivalent area

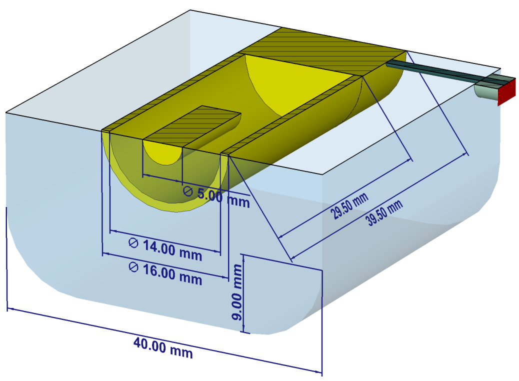

Figure 3.8: Resonator design dimensions

selected, because it allows to be hollowed out using a turning machine easily. Therefore, an absolute value of Q_0 could not be determined from Equation (2.66). Instead, a range of possible Q_0 values can be estimated, where the upper limit is the unloaded Q-factor of a structure completely made from the aluminum alloy and the lower limit a structure made completely from brass. Unfortunately, the electrical conductivity of brass, which was not known for the given material, is highly dependent on the amount of zinc (Zn) it contains. CST provides values for 91% copper (Cu) brass and 65% Cu brass, shown in Table 3.10.

Cu-Zn (%)	**σ (S/m)**
91-9	$27.4{\cdot}10^6$
65-35	$15.9{\cdot}10^6$

Table 3.10: Brass conductivity for 91% and 65% Cu brass

Following Equation (2.66), a range of Q_0 values between 957 and 1420 was found, where the lowest value would be in the case of the whole structure made from 65% brass and the best case for the whole structure made from highest conductivity aluminum alloy, listed in Table 2.2.

3.2.2 Simulations

The simulations were performed using CST Microwave Studio. The resonant frequencies of the individual resonators and the coupling bandwidths between them, obtained from the coupling matrix, had to be realized using actual 3-D structures. As a starting point for the models, the calculated resonator dimensions were used.

Resonant Frequency

A coaxial resonant cavity is constructed by using the chosen dimensions. The model is shown in Figure 3.9. The eigenmode solver was used for the simulation and all the metals

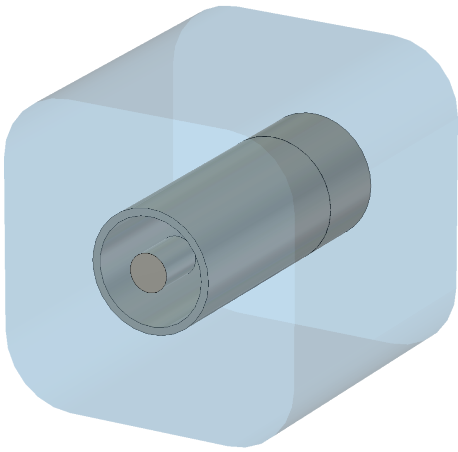

Figure 3.9: Single resonator model

were assigned to be PEC in order to limit the simulation time and required computational resources due to the complexity of the structure. Our goal was to obtain the tuning screw dependent resonant frequency. Therefore, a sweep over the screw length was done. The tuning screw was modeled as a simplified conductive cylinder. To determine the approximate range of screw lengths for the frequency values of the resonators, a coarse sweep from 0 mm, representing the resonant cavity without a tuning screw, to 16 mm was done. The maximum possible value is 30 mm, where the screw touches the bottom of the inner conductor. The inner conductor is not fully hollow to provide the possibility to mount it into the cavity using a screw. The coarse sweep simulation results are presented in Figure 3.10. The upper edge frequency f_U and lower edge frequency f_L are marked with

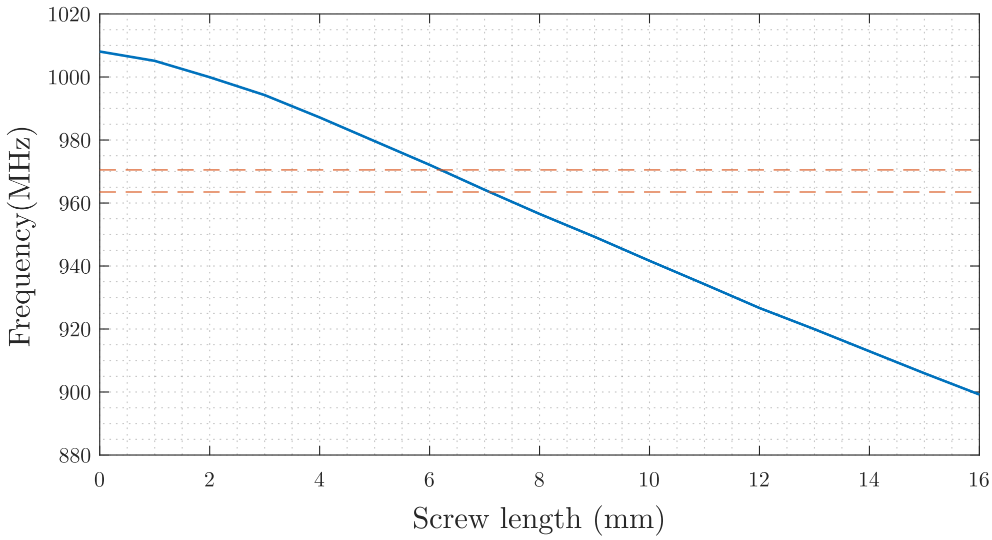

Figure 3.10: Resonant frequency simulation, coarse screw length sweep

a red dashed line to indicate the range of interest, since all resonant frequencies are in the passband. After the screw length range for our resonant frequencies was estimated, a finer sweep could be made in this range, to obtain screw length dependency of the resonant frequency. It was found that the frequency decreases approximately linearly with the screw length, which can be seen in Figure 3.11. A straight line was fitted over the simulated results to avoid the effects of simulation noise, and the slope of the linear equation was extracted from the results. In the figure, the three resonant frequencies of the resonators ($f_4 = f_1$) are marked along with their estimated screw lengths. The screw lengths are shown in Table 3.11. The parameters of the fitted linear equation, $y = k \cdot x + n$, were

no.	**screw length**
1	6.67 mm
2	6.89 mm
3	6.37 mm
4	6.67 mm

Table 3.11: Estimated tuning screw lengths to realize our resonant frequencies

found to be k=-7.74 MHz/mm and n=1018.46 MHz. They were noted for the full model tuning process.

External Coupling

The next step of the design was the simulation of the external coupling. As stated in Section 2.6, the external coupling can be altered with the height of the coupling probe,

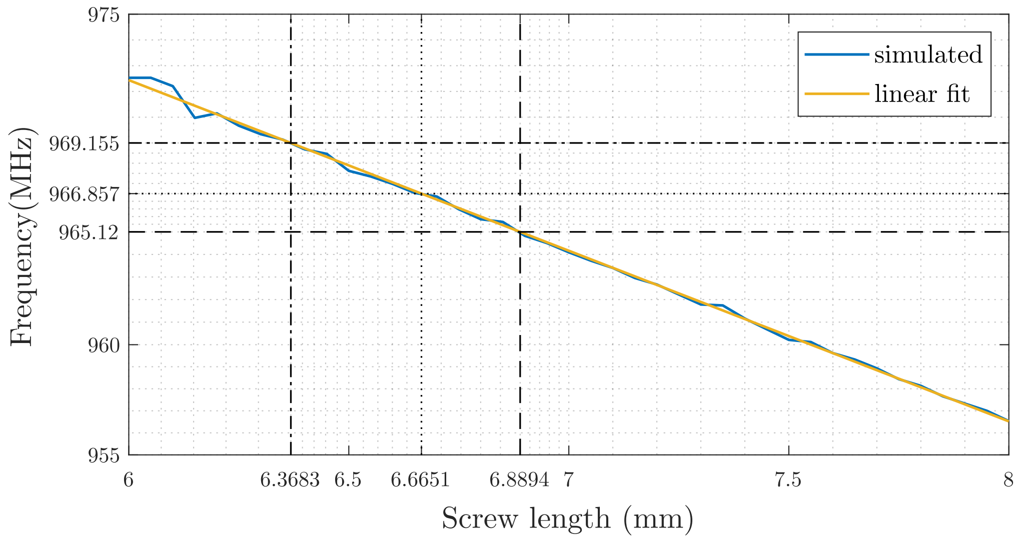

Figure 3.11: Resonant frequency simulation, fine screw length sweep

indicating the distance from the bottom, short-end of the resonator to the connector. A 50 Ω coaxial connector was created and placed at half-width of one of the cavity walls. The new model can be seen in Figure 3.12. To achieve desired coupling, the external Q-factor,

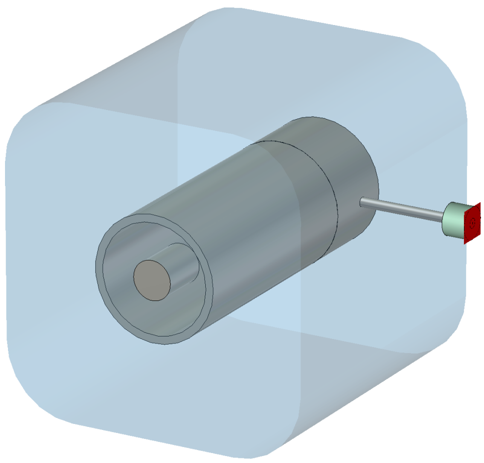

Figure 3.12: Single resonator model with probe

Q_{ext}, was determined by CST in the simulation. It was used to obtain the connector height dependent Q_{ext}. This was again done in two steps, starting with a coarse sweep from 1 to 10 mm. The coarse sweep results can be seen in Figure 3.13. The goal Q_{ext} is marked with a red dashed line, which suggest a connector height of approximately 4 mm. The fine sweep was therefore done closely around the value of 4 mm, with connector heights from 3.9 to 4.1 mm. From the fine sweep results, shown in Figure 3.14, the optimum connector height from the bottom of the cavity was found to be 4.016 mm. Due to limited precision in the manufacturing process, it was decided that a connector height of 4 mm will be used for future simulations and production instead.

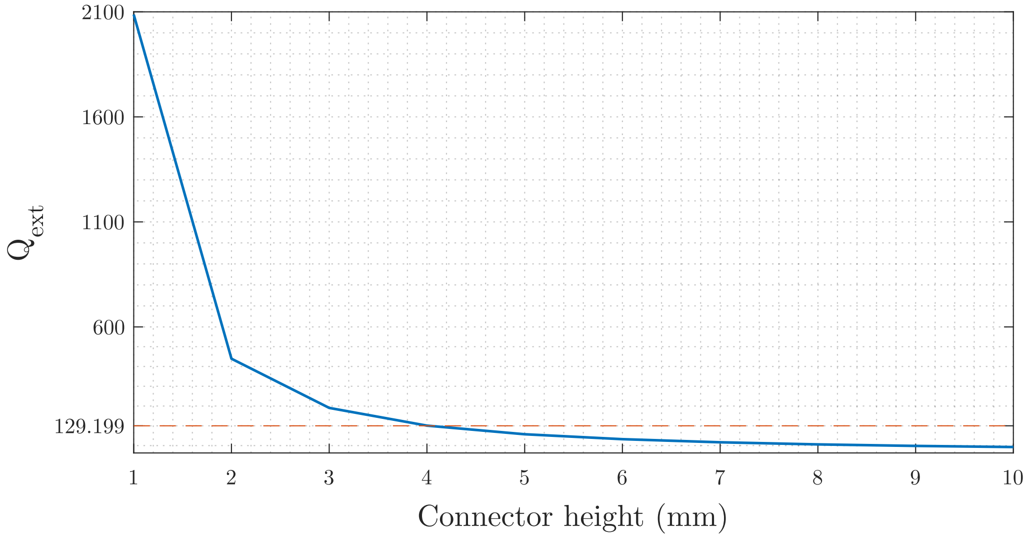

Figure 3.13: External coupling simulation, coarse connector height sweep

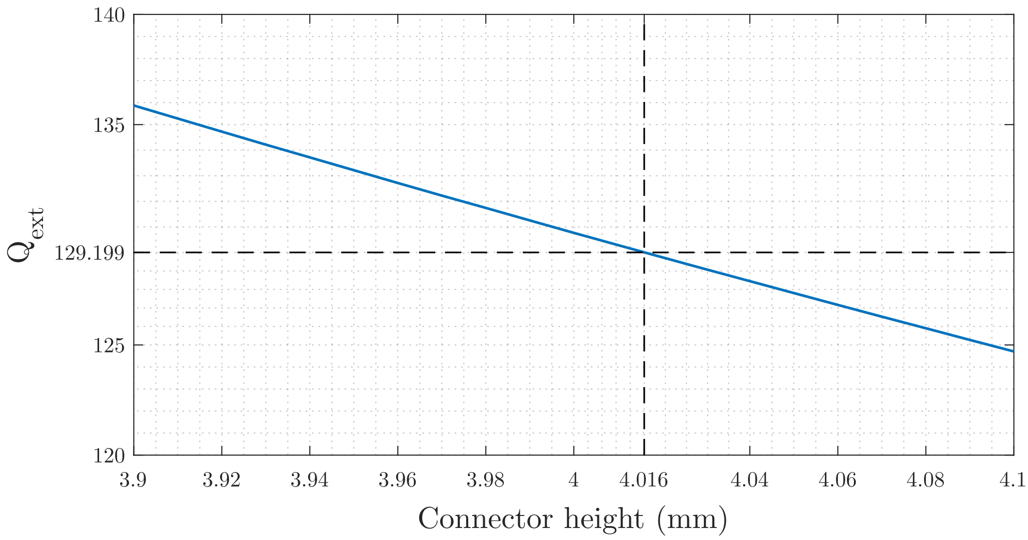

Figure 3.14: External coupling simulation, fine connector height sweep

Inter-Resonator Coupling

Theoretically, the simulation of the coupling between two resonators is independent of whether the two resonators are considered adjacent (mainline coupling) or non-adjacent (cross-coupling). The realization of couplings instead depends on whether magnetic or electric energy is coupled. In a realistic case, of course, both energies are coupled, but one is dominant, and based on it we separate energy coupling into inductive and capacitive coupling. In the coupling matrix, the inductive couplings have a positive value, while capacitive couplings have a negative value. The two couplings are commonly represented with a coupling bandwidth, which carries the sign of the coupling. In CST, the coupling bandwidth can be determined by $2 \cdot |f_1 - f_2|$, where f_1 and f_2 are the first and second resonant mode, determined by the eigenmode solver. This is an approximation, which is only valid for synchronously tuned resonators. In our example, the resonance frequencies of resonators are different. Therefore, to obtain the coupling bandwidths, the resonance frequencies of the two modes were obtained from the simulation results and Equations (2.14), (2.68) and (2.69) implemented in MATLAB [16].

Inductive Coupling

When talking about inductive coupling, the dominant field that is coupled between the resonators is magnetic. This can be realized in various ways, the simplest among them is putting an iris opening in the wall between the resonators. The inductively coupled resonators model is shown in Figure 3.15. The strength of the coupling is influenced

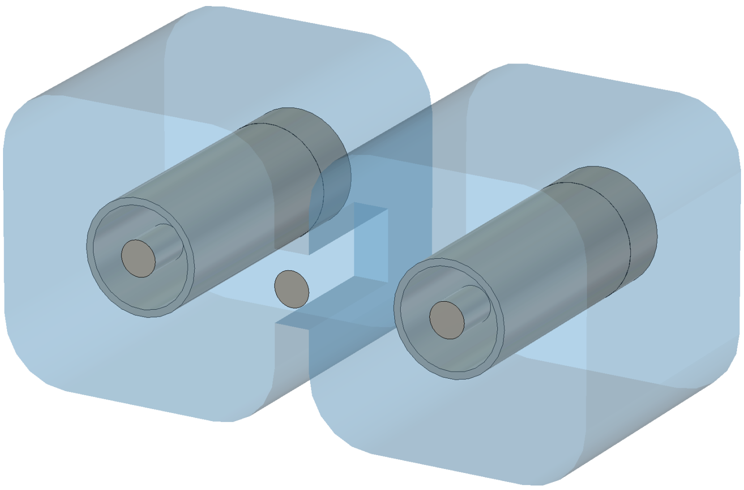

Figure 3.15: Inductive coupling model

by three parameters, the iris width, the iris depth, and most importantly, the tuning screw. Note that in the simulations, iris depth is represented by its inverse parameter, the minimum height from the bottom of the resonator, $h_{iris]}$. As for the case of the resonant frequencies, a tuning screw can be used to fine-tune the coupling bandwidth of an iris-coupled cavity pair. This means we can have multiple parameter combinations for the realization of the same coupling coefficient, therefore we have some freedom of choice when selecting the parameter values. The electric field and with it, the capacitive coupling component, is the strongest at the open end of the coaxial cavity. The tuning screw decreases the electric energy coupling and thus increases the overall magnetic coupling with increasing length. The magnetic field is stronger at the shorted end of the coaxial cavity, therefore a CBW decrease is expected for an increase of the minimum iris height. The depth was chosen as the first parameter for the sweep. The tuning screw was set to 0 length at this point, while the iris width was chosen to be 10 mm. Due to lack of literature, the iris width value was a guess choice. The sweep was done in the range from 0 to 20 mm minimum iris height, the results are shown in Figure 3.16. It was found that the simulation

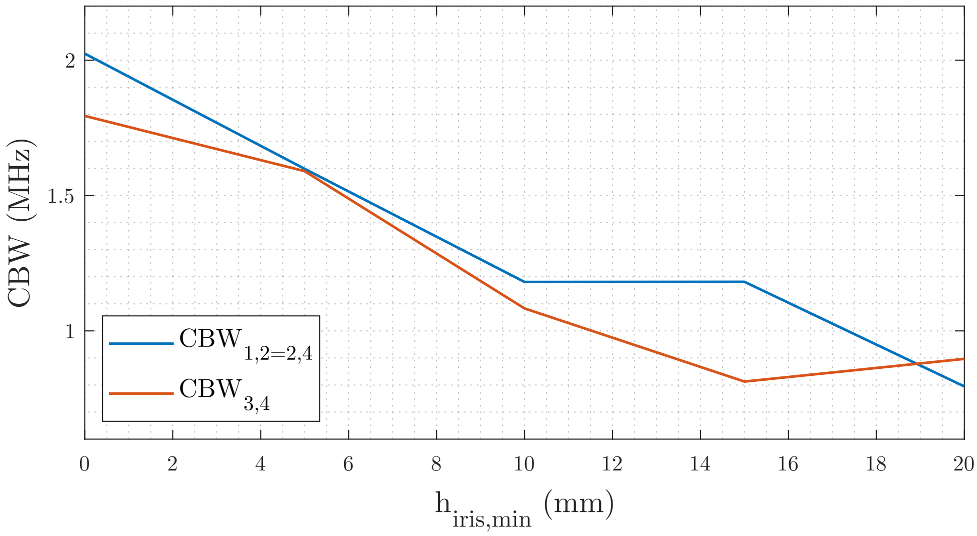

Figure 3.16: Inductive coupling simulation, minimum iris height sweep for resonator pairs 1-2 & 2-4 and pair 3-4 for w_{iris}=10 mm and $l_{\text{screw,iris}}$=0 mm

results tend to be somewhat unpredictable due to simulation noise. However the general influence of CBW decreasing with increasing minimum iris height was recognized. The CBW values in the whole sweep range were much smaller than the desired values, which indicated that other parameters certainly have to be modified. Although a minimum iris height of 0 mm shows itself as the best value based on the results of the sweeps, a height of 8 mm was selected for all three resonator couplings. This was done to provide additional structure strength, if, due to manufacturing issues, the filter would have to be manufactured with two covers. Coupling between resonator pairs 1-2 and 2-4 is the same, therefore only one of them had to be simulated in the following steps. Coupling between resonator pair 3-4 is different, so it had to be simulated individually. The next step was to determine the iris width for both of these couplings. The results of the sweeps can be seen in Figure 3.17. It was found that the influence of differently tuned resonators was small, both simulations giving a similar coupling bandwidth. For the iris width, values realizing coupling bandwidths smaller than the goal were selected. This way, the tuning screws, which increase the CBW, can be used for fine tuning. For resonator pairs 1-2 and 2-4, an iris width of 14 mm was selected, and for resonator pair 3-4, an iris width of 12 mm. The last parameter to be varied for fine-tuning the coupling bandwidth was the tuning screw. The tuning screw sweep for both depth-width pairs are shown in Figure 3.18. The parameters for the realization of desired the inductive couplings were estimated from the simulation sweeps in Figures 3.16 to 3.18. The estimations are listed in Table 3.12.

Capacitive Coupling

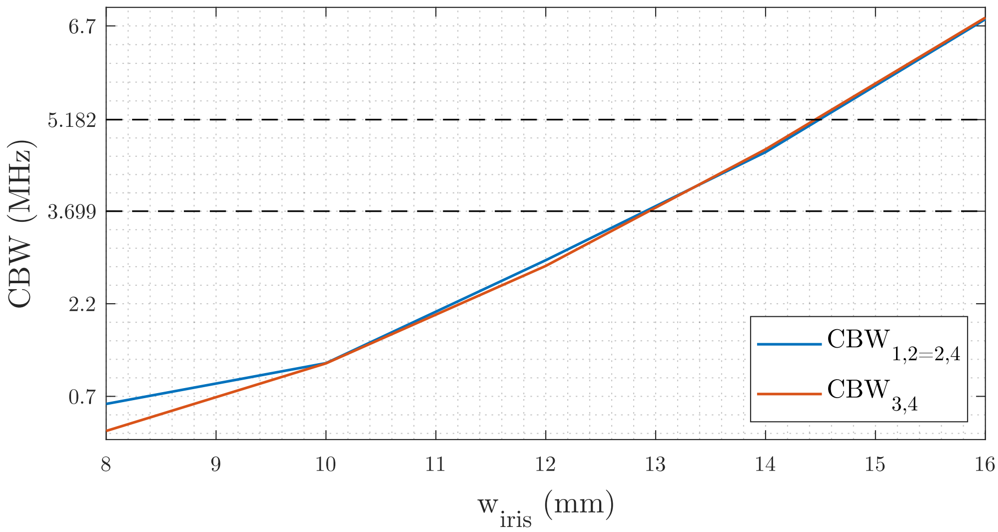

Figure 3.17: Inductive coupling simulation, iris width sweep for resonator pairs 1-2 & 2-4 and pair 3-4 for $h_{min,iris}$=8 mm and $l_{screw,iris}$=0 mm

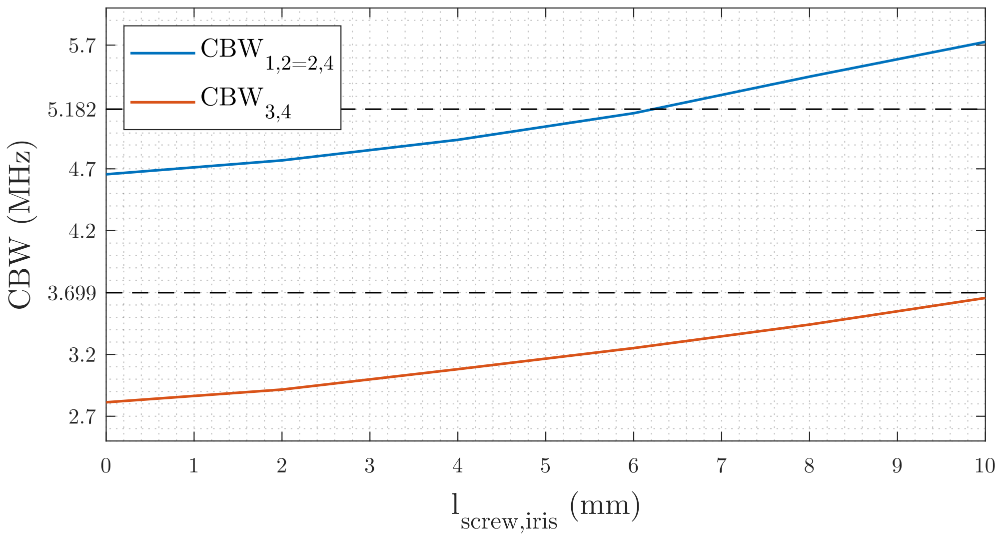

Figure 3.18: Inductive coupling simulation, iris tuning screw sweep for pairs 1-2 & 2-4 and pair 3-4

res. pair	$h_{min,iris}$	w_{iris}	$l_{screw,iris}$
1-2	8 mm	14 mm	6.2 mm
2-4	8 mm	14 mm	6.2 mm
3-4	8 mm	12 mm	10 mm

Table 3.12: Estimated inductive coupling parameters for all inductive couplings

In the case of capacitive coupling, the dominant coupled energy is electric. The electric field in a quarter - wavelength coaxial resonator is the strongest at the open end of the resonator, therefore the capacitive coupling mechanism is implemented on that side. The mechanism is realized with a conductive probe approaching the inner conductors of both resonator cavities. This requires a small hole in the wall between the cavities. A dielectric is used to hold the probe in place. The model can be seen in Figure 3.19. The capacitive

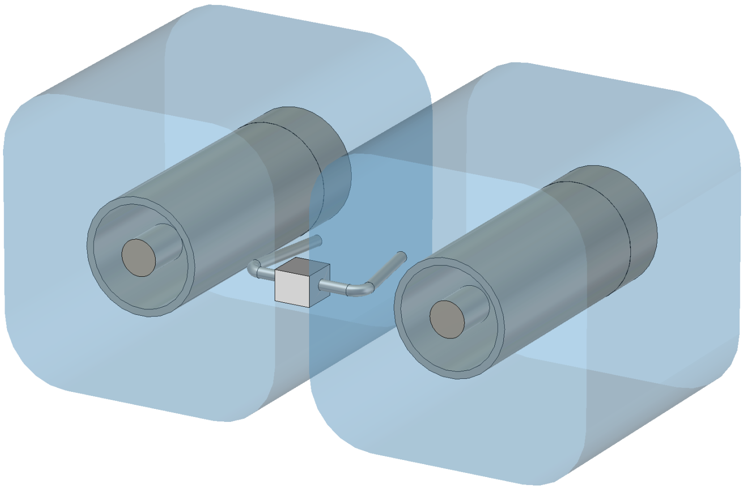

Figure 3.19: Capacitive coupling model

coupling is the most demanding mechanism in the filter. Tuning screws are not applicable in this setup, limiting the tunability of the setup. Many various methods of realization exist, with different probe shapes. The idea behind the used design was to use a simple copper wire (with a diameter of 1.5 mm) as the coupling probe, which can easily be bent. The parameters that affect the coupling bandwidth in this case are the length of the horizontal part of the copper wire, the length of the bent parts, and the angle at which these parts are bent. The first two parameters were considered as the initial parameters, which had to be determined first. Due to lack of literature, we started with setting the parameters to initial best-guess values, which were to be validated during simulations. The bending angle was set to $\alpha = 90°$ and the vertical probe length to 12 mm. The sweeps of the horizontal probe length is shown in Figure 3.20. Since three parameters are available for the capacitive coupling, at this point an approximate value convenient to manufacture was selected, i.e. 13 mm. Using this value, a vertical probe length sweep followed around the value selected for the previous simulation. The bending angle was kept at $\alpha = 90°$ in this step as well. The simulation results are plotted in Figure 3.21. Again, for the ease of production, an approximate value of 12 mm was selected. The bending angle was then varied to find the optimal coupling bandwidth. This is presented in Figure 3.22. From the three parameter sweeps, the approximate parameters for the capacitive coupling were

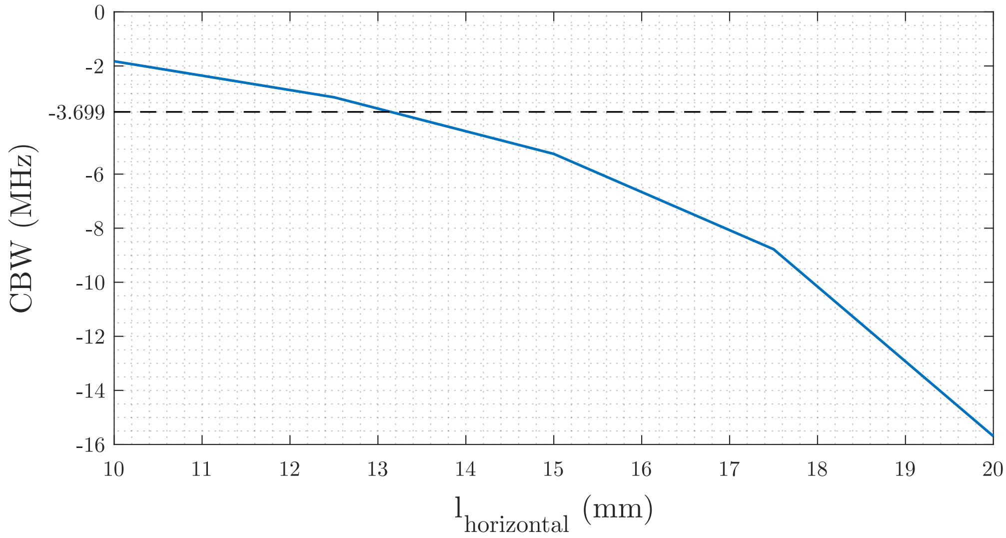

Figure 3.20: Capacitive coupling simulation, horizontal probe length sweep for l_{vertical}=12 mm and α=90°

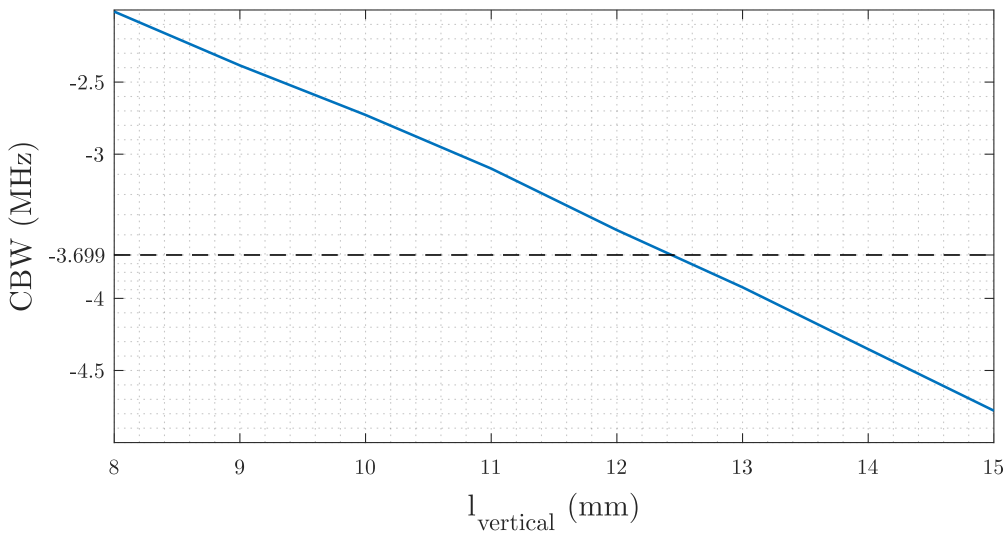

Figure 3.21: Capacitive coupling simulation, vertical probe length sweep for $l_{\text{horizontal}}$=13 mm and α=90°

determined: $l_{\text{horizontal}} = 13\ mm$, $l_{\text{vertical}} = 12\ mm$, and $\alpha = 88.5°$. Determining the values more precisely at this point is not needed, since the precision of the handmade production of the coupling probe is severely limited.

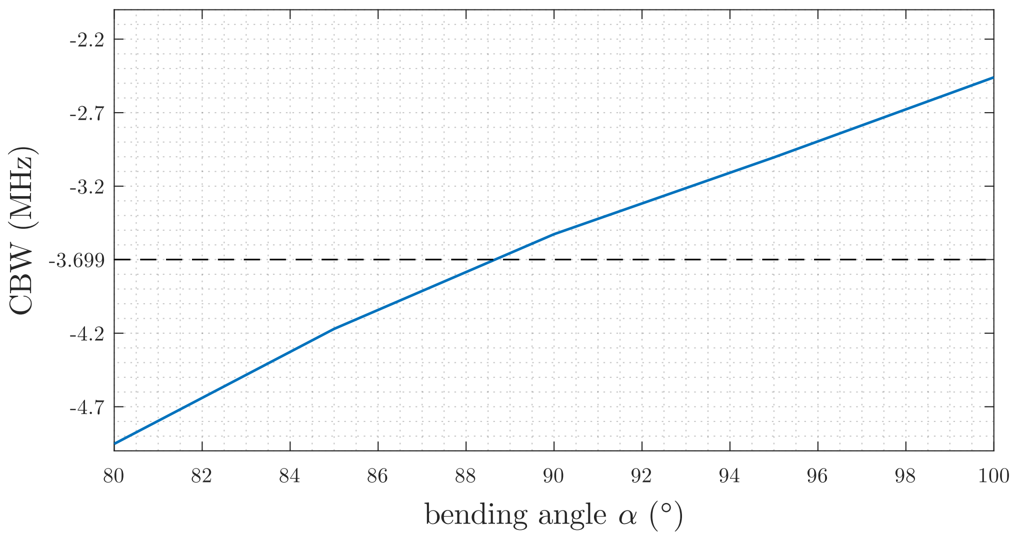

Figure 3.22: Capacitive coupling simulation, probe angle sweep for l_{vertical}=12 mm and $l_{\text{horizontal}}$=12 mm

Full Model

In the previous sections, physical models of all the coupling matrix elements were created by using simulations with parameter sweeps. The full model was now built by joining all the segments together. The idealistic materials (PEC and lossless teflon) were replaced with the materials which were going to be used for the manufacturing process. The eigenmode solver was now replaced with the frequency domain solver and two ports were defined on the source and load connectors. With these settings, the structure could now be simulated to obtain the full model S-parameters. The full model can be seen in Figure 3.23. The position of each of the coupling mechanisms is determined from the coupling matrix structure in Table 3.7. When joining all of the individual segments to a full model, the segments influence each other and are consequently detuned. In the simulation, detuned S-parameters were obtained, which are portrayed in Figure 3.24. The S-parameters from the detuned model were imported into CST Filter Designer 3D. Using this software, a coupling matrix can be extracted from the S-parameters. It also shows the offset percentages for all of the coupling matrix elements. The filter model now had to be tuned to compensate for these detuning effects, caused by joining all segments of the filter. From the sweep results in the previous sections, the required changes for all tuning screws and the angle of the capacitive coupling probe were estimated. Since every parameter change influences all the other values, this was done in steps. In the first step, the resonator tuning screws were tuned. Tuning of the inductive coupling tuning screws followed in second step. In the last, third step, the capacitive coupling probe angle was tuned.

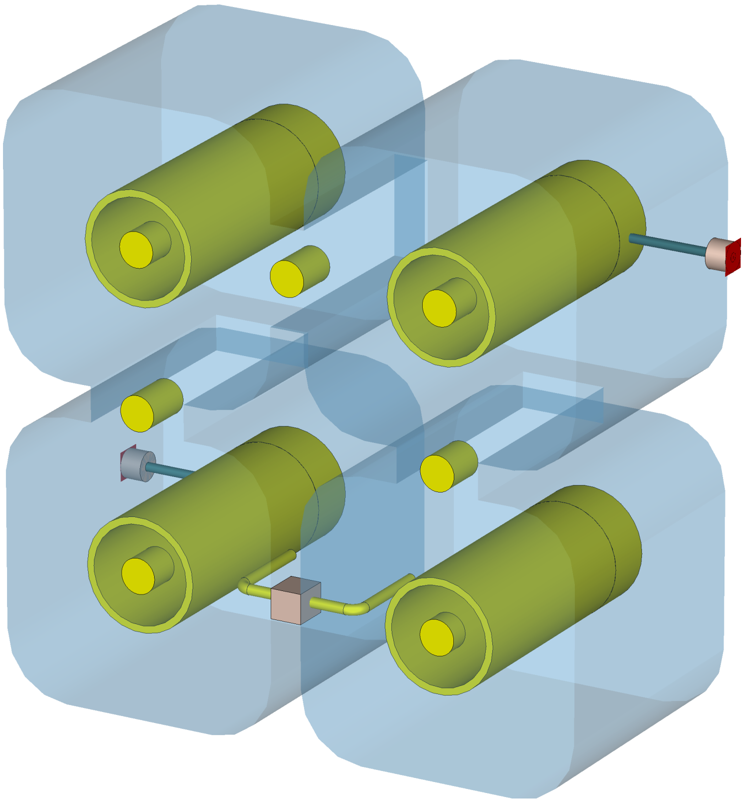

Figure 3.23: Full filter model

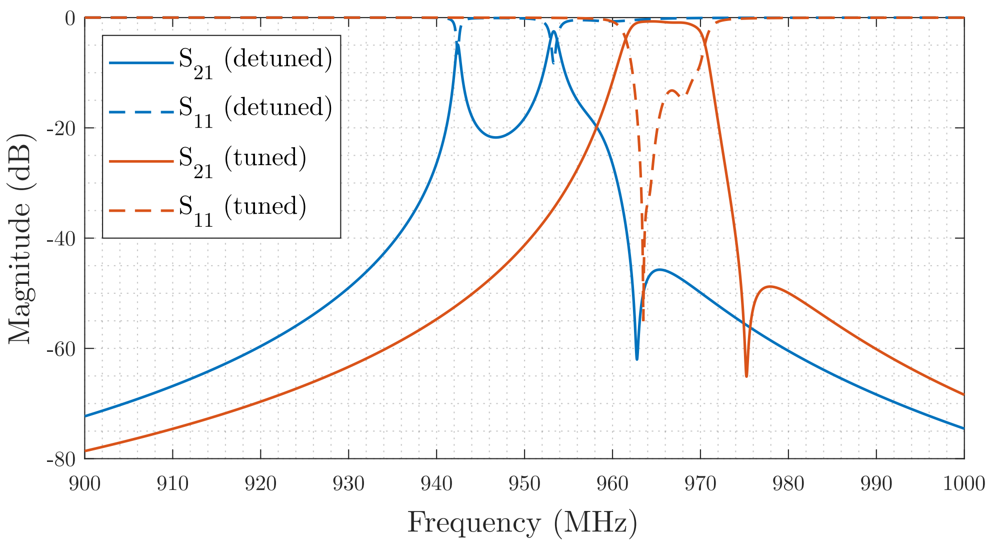

Figure 3.24: Full model simulation, detuned and tuned filter S-parameters

3.2.3 Production

The tuning of the full filter model during simulation is not unconditionally necessary in order to manufacture the filter, since the tuning can more easily be done on the actual physical model while measuring the S-parameters. However, it gives us initial values of the tuning elements, which ideally should work the same in a real model, but more realistically, it is a good starting point for the tuning, due to the limited precision of the manufacturing process and possible human errors. The manufactured model is shown in Figure 3.25, while technical drawings of the manufactured structure are given in Appendix A. The more

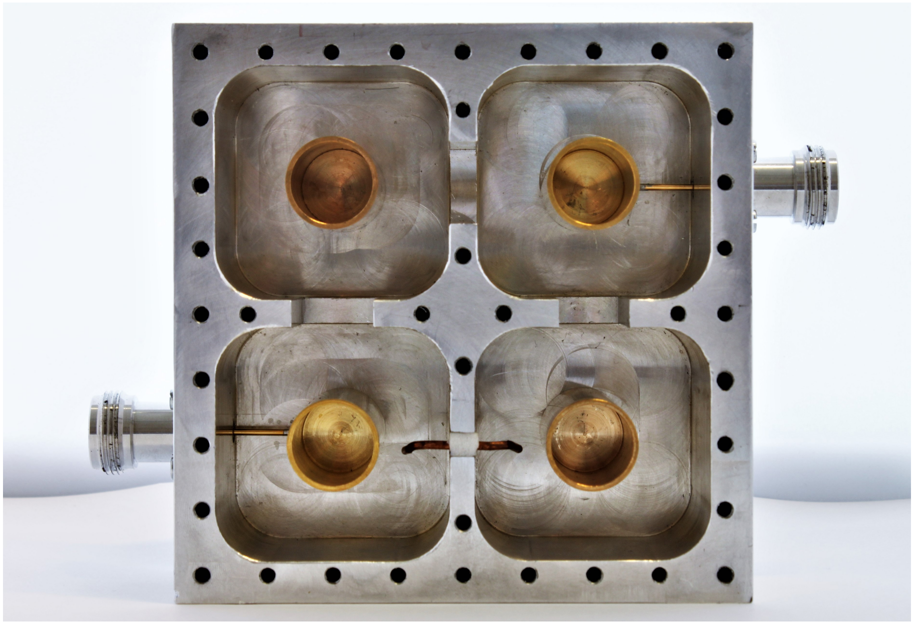

Figure 3.25: Complete filter

robust type N connectors were mounted to the filter, the dielectric was cut to the inside walls of the resonant cavities and the inner conductors, made from brass, were mounted into the cavity using submersible screws in the bottom of the filter. The connectors need to be electrically well connected to the inner conductors to obtain the external Q-factor which was simulated. Therefore, they had to be soldered. This process was especially difficult due to the large dimensions of the filter, which had to be heated sufficiently for the solder to attach to the inner conductors. A mistake was done during the manufacturing process, causing one dimension of cavity 3 to be 0.55 mm larger than initially designed, with the wall between cavity 1 and cavity 3 being 0.55 mm smaller than other walls. The inner conductor was placed aligned with other conductors. The manufactured filter was not discarded, instead the effects of this mistake on the complete filter were investigated with some post-production simulation steps. It was discovered, that the filter can still be tuned to the desired operation. The tuning screws and the capacitive coupling probe were set to the tuned simulation result parameters. This gave us a detuned result. The measured S-parameters were saved, imported, and the coupling matrix was extracted in CST Filter Designer 3D, following the same procedure as for the simulation results. Then, the screw lengths and the angle of the capacitive probe were adapted using the simulated sweeps. This was repeated three times until a satisfiable result was found. The initial setup and the tuned setup can be seen in Figure 3.26. As a final processing step, the

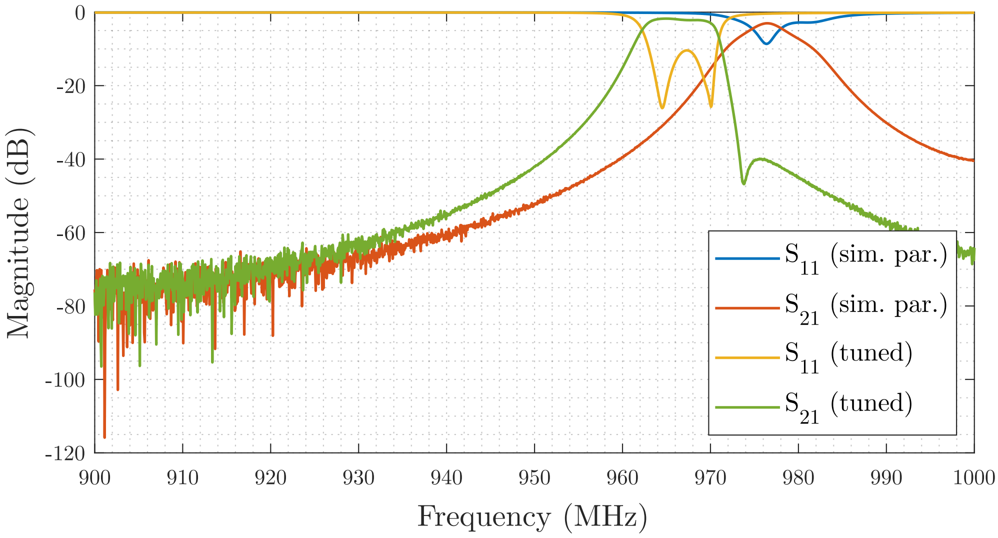

Figure 3.26: Tuning of the filter

filter was sent to be silver-plated. After silver-plating, it was measured in two different setups, once using brass inner conductors and once using silver-plated inner conductors. The silver-plated filter with silver-plated inner conductors is shown in Figure 3.27.

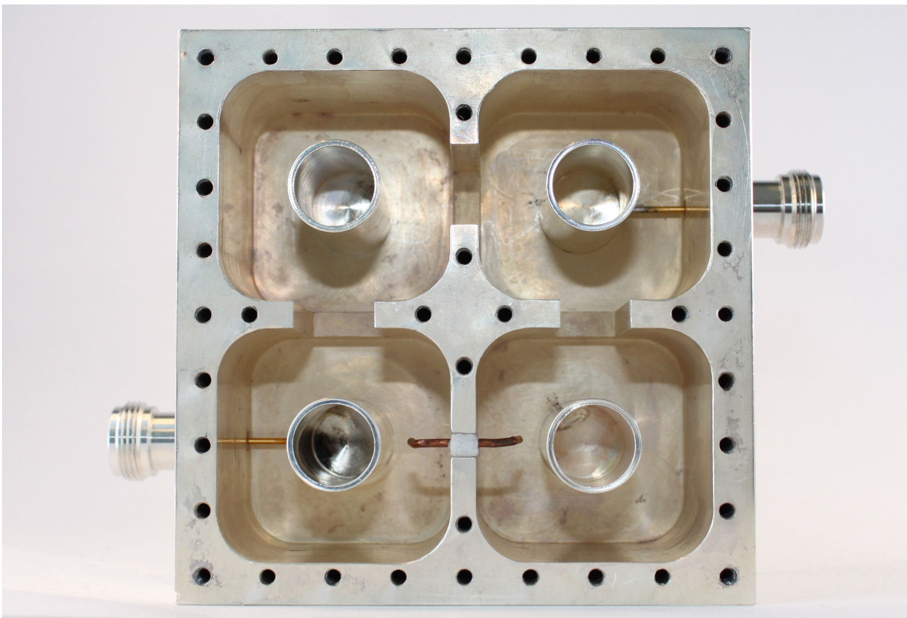

Figure 3.27: Complete filter after silvering

4 Measurements and Post-Processing

After designing and manufacturing the bandpass filter and the resonant cavities, it is now required to do the measurements and the post-processing of these measurements to obtain comparable results. This chapter deals with these two segments of the thesis.

The first part focuses on the measurements and the measurement equipment used. This is described in Section 4.1. The measurements were done with a VNA and the results given in the form of scattering parameters. After that, these S-parameters have to be processed to obtain the desired results. Since the required results in the case of a BPF are S-parameters, which directly allow the evaluation of filter characteristics, no post-processing steps are required in this case. The unloaded Q-factor, on the other hand, has to be determined from the complex reflection parameter, which is the focus of Section 4.2 of this chapter.

4.1 Measurements

The required measurements for both the filter and the resonant cavities were standard S-parameter measurements with a VNA, specifically the Agilent PNA E8364A. The measurement process is well known and will therefore not be described in detail. The focus is on stating the measurement settings, the frequency range etc.

4.1.1 Resonant Cavities

In the case of resonant cavities, female SMA connectors were used, which can be used at a wider frequency range than the type N connectors (up to 18 GHz in comparison to type N, which typically operate up to 11 GHz). Resonant cavities were designed only with one port, so a one-port SOL (Short-Open-Load) calibration with the HP 85052D calibration kit was done, using the female connector set, since the used DUT connectors were also female. The measurements, and therefore also the calibrations, were done in two frequency ranges, one from 0 Hz to 18 GHz, which is the operation range of the SMA connectors, and the other range with a 1 GHz span around the first resonance frequency, which was found to be at approximately 8.833 GHz. In both cases, the IF bandwidth of 1 kHz was used to obtain a good resolution of the very narrow resonances. The number of points was set to the maximum, 20 001, in both cases, for the larger frequency band it was simply necessary due to the large bandwidth. In the 1 GHz frequency band, it was done in order to have a small frequency step, which is important around the resonance frequencies for the post-processing steps done on these measurement results.

4.1.2 Bandpass Filter

The bandpass filter operates at the L frequency band, its passband designed to be in the range between 963.5 MHz and 970.5 MHz. At such low frequencies, type N connectors can be used, which are larger and more robust than the SMA connectors. Female type N connectors were used. The calibration was therefore done with the female HP 85032B type N calibration kit. Understandably, since the filter is a two port device, a two-port SOLT (short-open-load-through) calibration was done. The frequency range of the measurement was selected to be between 900 MHz and 1000 MHz. A detuned filters resonances can be offset far from the desired passband so a smaller frequency range would be very impractical when tuning the filter. To avoid too long measurement times, which would make the screw tuning harder, 1601 measurement points were selected. As in the resonant cavities case, the IF bandwidth of the VNA was reduced to 1 kHz to achieve a good resolution.

4.2 Post-Processing

As mentioned before, the goal of the resonant cavity measurements was to obtain its unloaded Q-factor. Two methods for calculating Q_0 from measured S-parameters were described in Section 2.3. Both methods assume negligible losses of the coupling mechanism and attempt to fit the measured data in a narrow frequency band around the resonance. To avoid these limitations, a new model is proposed, which develops an equivalent circuit model of the resonator, together with some effects of the nonideal couplig mechanism and an error minimization algorithm to fit the model to the measured results. The minimization algorithms convergence strongly depends on the initial parameter values, which have to be estimated before running the algorithm. Because of the simplicity and computation speed of the algorithm proposed in [10], it was used as a starting point to obtain the initial parameter values.

The new proposed circuit model, shown in Figure 4.1, assumes an additional 50 Ω transmission line of length l, a series inductance due to the connector, L_C, and a parallel connector capacitance, C_C. The additional transmission line attempts to model the 50 Ω line of the SMA connector from the reference plane of the measurement to the inner wall of the cavity. It is modeled as lossless, while the losses are considered in the real part of the coupling mechanism. The series inductance and parallel capacitance are parasitic effects which originate from the mathematical model of the SMA connector, as described e.g. in [17]. It was observed that they can be used to incorporate the reflection fluctuation in the frequency range far from the resonance frequency. The input impedance is calculated in steps, starting at Z_1 and adding components until Z_{in} is reached. The steps for calculating

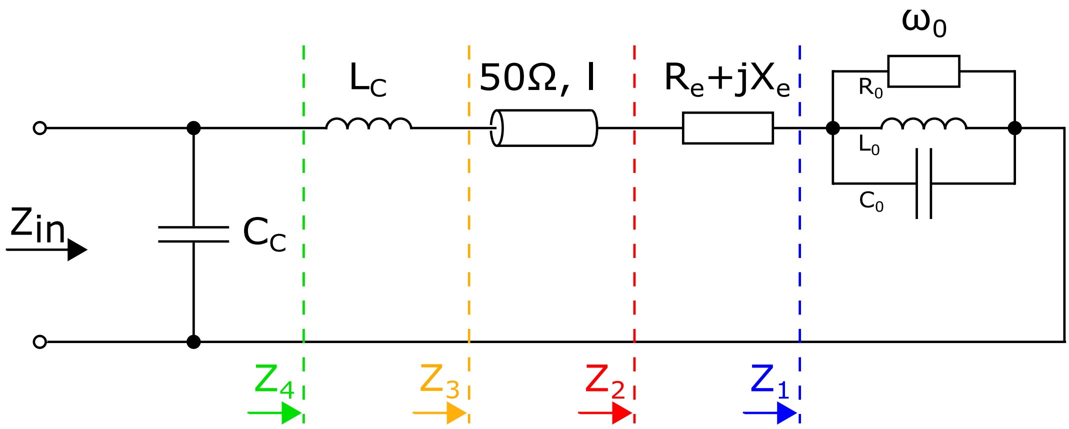

Figure 4.1: Proposed expanded model of a resonant cavity

the input impedance, marked in Figure 4.1, are

$$\begin{aligned}
Z_1 &= \frac{R_0}{1 + jQ_0\left(\frac{f}{f_0} - \frac{f_0}{f}\right)}, \\
Z_2 &= Z_1 + \left(R_e + j\frac{X_e}{1+\psi}\right), \\
\Gamma_2 &= \frac{Z_2 - Z_0}{Z_2 + Z_0}, \\
\Gamma_3 &= \Gamma_2 \cdot e^{\frac{-j4\pi f l\sqrt{\varepsilon_r}}{c_0}}, \\
Z_3 &= Z_0 \cdot \frac{1+\Gamma_3}{1-\Gamma_3}, \\
Z_4 &= Z_3 + j2\pi f L_C, \\
Y_{in} &= \frac{1}{Z_4} + j2\pi f C_C, \\
Z_{in} &= \frac{1}{Y_{in}}.
\end{aligned} \tag{4.1}$$

The reflection coefficient can then be expressed from Z_{in} as

$$\Gamma_{in} = \frac{Z_{in} - Z_0}{Z_{in} + Z_0}. \tag{4.2}$$

This coefficient should now be fitted to match to the measured results. For the initial values, Q_0, f_0, R_0, and X_e from the method in [10] are selected, where f_0 is simply assumed to be f_L. The length of the connector up to the inner cavity wall was measured and estimated to be approximately $l = 11\ mm$. The coupling losses, represented with R_e were assumed small, a value of 0.2 Ω was selected as the starting value. The parasitic effects of the connector, together with the additional line length, cause a shift of the resonant frequency and can cause a circle to appear fitted to the values, which has a very high error due to the shift of the resonant frequency. The starting values were estimated experimentally to assure convergence of the algorithm. This was done using NI AWR Microwave Office [18], by modifying the parameter values to match the results. It was found that the influence of the parasitic capacitance is negligible, while the parasitic inductance is detrimential for the behavior of the circuit. The initial parasitic series inductance was selected to be $L_C \approx 0.1\ nH$.

In the next step, the error minimization algorithm follows. The mean squared error (MSE) between the measurement results and the model reflection coefficient is defined, which is used as the input for the minimizing algorithm, MATLABs `fminsearch` function. The optimization of the parameters is separated into multiple steps, where the first step attempts to fit the line length l, the second step fitts the resonant cavity parameters, the third step the coupling parameters, the fourth step the parasitics of the connector, and in the final, fifth step, all the resulting optimized parameters are input to the optimizer for the final optimization. A common issue with optimizing algorithms is the problem of the order of variables being very different. To avoid this, all the parameters input to the function were normalized. To avoid parameter sign switching, which could result in nonphysical values, a penalty value was added to the MSE in such cases. An example Smith chart plot of the results of the optimization steps is shown in Figure 4.2.

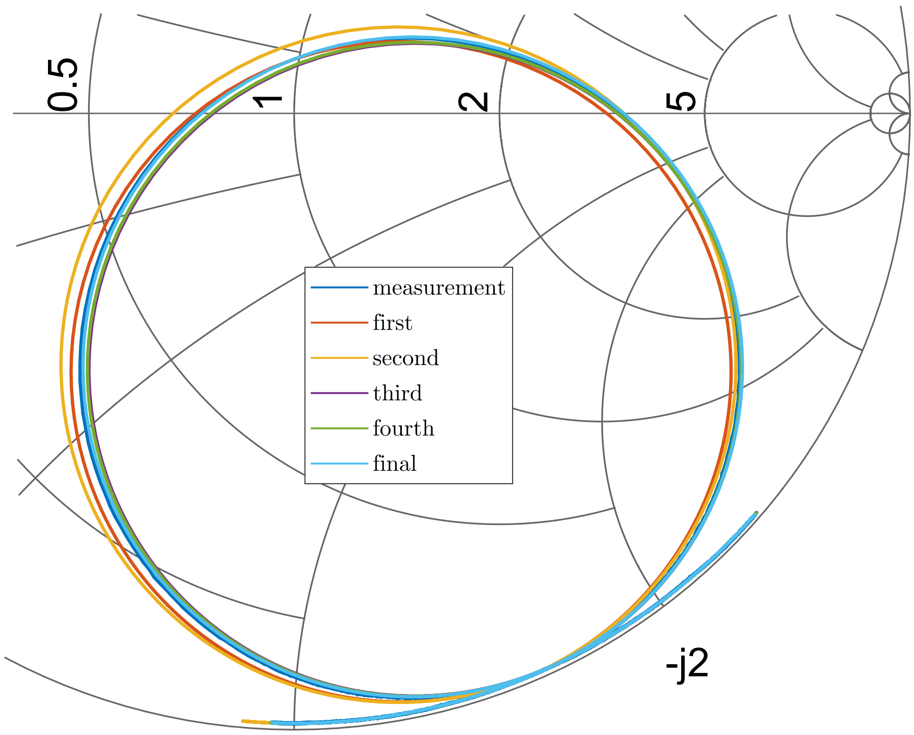

Figure 4.2: Results of optimization by steps

5 Results

In this chapter all the results obtained in the scope of this thesis are presented. It aims to present the results of the measurements and draw a comparison between them and the results obtained analytically and/or from simulations. Again, the results are divided into two major sections.

In Section 5.1, all the results for the evaluation of the unloaded Q-factor are presented. The results obtained from the newly created model are compared to the two techniques proposed in [3],[10]. The second section, Section 5.2, presents the BPF results. The coupling matrices for three different material setups along with their offsets from the synthesized matrix are shown. The reduction of losses due to silver-plating is presented graphically, as an insertion loss comparison, and as Q_0 estimations by CST FD3D,.

5.1 Q_0 of a Resonant Cavity

To observe the difference between the manufactured cavities, the measured S-parameters were compared firstly, shown in Figure 5.1. It can be seen that for the same connector, the results between the cavities vary in the range of tens of MHz. The differences were found to be caused by small differences in cavity dimensions and, partially, the changes in the cavity wall thickness, which resulted in a variation of the length of the connector inside the cavity. Afterwards, the effect of different connector lengths on the reflection parameter was observed. Figure 5.2 shows the comparison between the three selected connector lengths. Connector 1 (l = 6.42 mm) is approximately optimally coupled. This results in a return loss of more than 20 dB. Connector 2 (l = 7.82 mm) has caused a very weak overcritical coupling with approximately 2 dB return loss at the loaded resonant frequency. The third connector, connector 3 (l = 5.76 mm), resulted in an undercritical coupling, which was, with around 6 dB return loss, stronger than the undercritical case.

These measured results were now processed using the new proposed method, presented in Section 4.2. From the MATLAB script implementation of the method, the Q_0 results were obtained for all three cavities. They are listed in Table 5.1. Since the resonant frequencies are still very close to each other, it was expected that Q_0 results will remain similar for all three cavities. These expectations were confirmed and the variation coefficient of Q_0 from the mean value for the three cavities was less than 0.4 %.

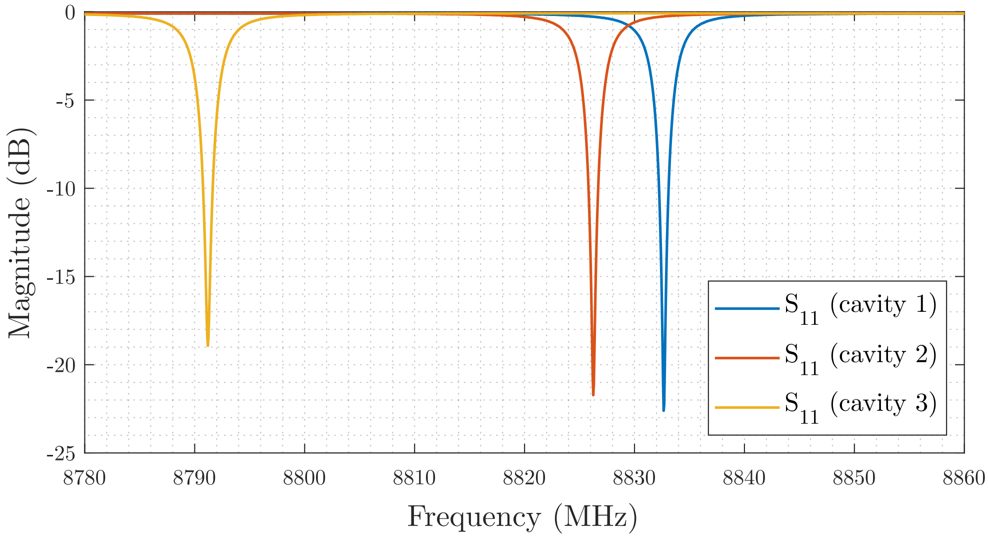

Figure 5.1: Comparison between the three cavities (connector 1)

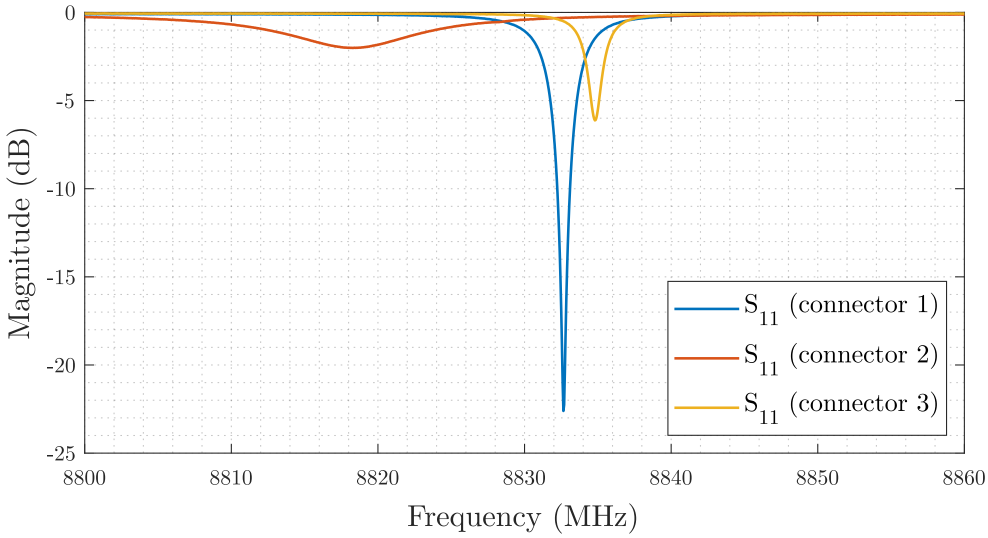

Figure 5.2: Comparison between different connector lengths (cavity 1)

measurement	connector 1	connector 2	connector 3	mean
cavity 1	7215.7	7180.4	7211.4	*7202.5*
cavity 2	7190.4	7135.7	7155.1	*7160.4*
cavity 3	7178.7	7269.8	7167.7	*7208.4*
polished 1	7413.5	7343.5	7414.6	*7390.5*
silver-plated 2	5327.5	5315.6	5324.3	*5322.5*
silver-plated 3	9572.4	9611.2	9546.0	*9576.5*

Table 5.1: Q_0 results

5.1.1 Polishing

Cavity 1, which had a visually rougher surface than cavity 2, was selected to be polished. The unloaded Q-factor of the polished cavity is also listed in Table 5.1. A small improvement of Q_0, 2.6%, was observed when comparing the results to the unpolished results of cavity 1.

5.1.2 Silver-Plating

The Q_0 results for the silver-plated cavities 2 and 3 are also listed in Table 5.1. The results for cavity 2 indicate a deterioration of Q_0 for silver-plating, which does not agree with the theoretical expectations. The silver-plating process has increased the losses in the cavity. It was found that the the silver layer was poorly contacted with the aluminum alloy cavity. A less conductive layer of nickel was used between the cavity surface and the silver layer. The middle layer is needed to disperse the silver layer on the structure, because a direct joining of the two materials at hand is difficult. During this process, something probably went wrong. The results of the silver-plated cavity 3 show a more realistic effect of silver-plating the cavity. Here, a layer of copper was used under the silver layer. A good electrical connection was obtained. Q_0 increase of 33% in comparison to the non-silver-plated cavity was observed. In Section 2.4, the theoretically expected range was found to be between 34% and 50%. Our measurement thus coincides with the analytically expected values.

5.1.3 Comparison with Other Methods

A comparison of Q_0 results and their variation for different coupling coefficients was done to establish the quality of the proposed method. The results can be seen in Tables 5.2 and 5.3. The variation coefficient of the proposed method is found to be close to a factor

	variation coefficient $\left(\frac{\textbf{variance}}{\textbf{mean}}\right)$						
method	**cav. 1**	**cav. 2**	**cav. 3**	**pol. 1**	**sil.pl. 2**	**sil.pl. 3**	**avg. var**
Kajfez [3]	3.0%	3.2%	1.2%	3.0%	3.2%	3.3%	2.8%
Shahid [10]	3.6%	3.6%	2.4%	3.8%	2.7%	3.8%	3.3%
new method	0.3%	0.4%	0.8%	0.6%	0.1%	0.3%	0.4%

Table 5.2: Comparison of Q_0 variation results with other models

method	mean Q_0 cav. 1	cav. 2	cav. 3	pol. 1	sil.pl. 2	sil.pl. 3
Kajfez [3]	7010.4	6964.1	6977.5	7245.1	5205.3	9258.8
Shahid [10]	7016.5	6957.2	6990.1	7200.7	5197.1	9236.5
new method	7202.5	7160.4	7205.4	7390.5	5322.4	9576.6

Table 5.3: Comparison of mean Q_0 results with other models

10 smaller than the two presented existent methods. Additionally, it can be seen that the Q_0 values are somewhat higher than for the other two methods. This is mainly due to the fact that the coupling mechanism losses are considered in the proposed method, whereas the other two methods assign these losses to the unloaded Q-factor. Thus, it was found that the results, obtained from the new proposed method, are more accurate and more stable than the results obtained from the other two methods.

5.2 Bandpass Filter

The S-parameters of the filter were measured for three different setups. First with aluminum structure and brass inner conductors, second with silver-plated structure and brass inner conductors, and the third with both the filter housing and the brass inner conductors silver-plated. In all cases, the parameters of the BPF had to be tuned. The sequential tuning process, presented in Section 3.2.3, was used and repeated until the deviations from the synthesized coupling matrix coefficients were below 10%. With the first setup, before silver-plating, the extracted coupling matrix results for the final tuned model were offset for 8.2 % or less. The extracted matrix of the tuned filter, along with the offset percentages from the initial design, is shown in Table 5.4. The extraction interval, i.e. the

	S	**1**	**2**
S	0.000	0.992 (-4.0%)	0.000
1	0.992 (-4.0%)	0.089 (-2.5%)	0.754 (+1.8%)
2	0.000	0.754 (+1.8%)	0.437 (+4.9%)
3	0.000	-0.555 (+5.0%)	0.000
4	0.000	0.000	0.767 (+3.6%)
L	0.000	0.000	0.000
	3	**4**	**L**
S	0.000	0.000	0.000
1	-0.555 (+5.0%)	0.000	0.000
2	0.000	0.767 (+3.6%)	0.000
3	-0.770 (-3.7%)	0.507 (-4.0%)	0.000
4	0.507 (-4.0%)	0.203 (-8.2%)	0.992 (-4.0%)
L	0.000	0.992 (-4.0%)	0.000

Table 5.4: Extracted coupling matrix of the manufactured model - aluminum/brass

frequency interval of extraction, strongly influences the results. CST recommends that the interval captures all transmission zeroes while remaining as small as possible. An interval from 955 MHz to 980 MHz was used in this example and in the two following extraction cases as well. For the second material combination, the silver-plated cavity walls and brass inner conductors, the extracted matrix of the tuned filter, along with the offset percentages from initial design, is shown in Table 5.5. For the third material combination, silver-plated filter with silver-plated inner conductors, the extracted matrix of the tuned filter, along with the offset percentages from initial design, is shown in Table 5.6. For the from S-parameters extracted coupling matrix, CST Filter Designer 3D provides an estimation of uncoupled resonators Q_0. The comparison between all three filter material combinations is listed in Table 5.7. These estimates give us an indication of the improvement due to the silver-plating of the filter. The factor of improvement between the start model and the completely silver-plated model is approximately 2.2. A comparison of scattering parameters of all the material combinations and the original synthesized result can be seen in Figure 5.3. Although the coupling matrix coefficients do not indicate large differences in filter tuning, the results in Figure 5.3 lead to the conclusion that the

	S	**1**	**2**
S	0.000	1.023 (-1.1%)	0.000
1	1.023 (-1.1%)	0.070 (-1.5%)	0.741 (+0.03%)
2	0.000	0.741 (+0.03%)	0.628 (-4.6%)
3	0.000	-0.488 (-7.7%)	0.000
4	0.000	0.000	0.753 (+1.7%)
L	0.000	0.000	0.000
	3	**4**	**L**
S	0.000	0.000	0.000
1	-0.488 (-7.7%)	0.000	0.000
2	0.000	0.753 (+1.7%)	0.000
3	-0.803 (-2.1%)	0.518 (-1.9%)	0.000
4	0.518 (-1.9%)	0.006 (+1.7%)	1.023 (-1.1%)
L	0.000	1.023 (-1.1%)	0.000

Table 5.5: Extracted coupling matrix of the manufactured model - silver/brass

	S	**1**	**2**
S	0.000	1.001 (-3.2%)	0.000
1	1.001 (-3.2%)	0.048 (-0.46%)	0.734 (-0.84%)
2	0.000	0.734 (-0.84%)	0.532 (+0.2%)
3	0.000	-0.491 (-7.0%)	0.000
4	0.000	0.000	0.745 (+0.59%)
L	0.000	0.000	0.000
	3	**4**	**L**
S	0.000	0.000	0.000
1	-0.491 (-7.0%)	0.000	0.000
2	0.000	0.745 (+0.59%)	0.000
3	-0.841 (-0.18%)	0.528 (-0.15%)	0.000
4	0.528 (-0.15%)	0.042 (-0.14%)	1.001 (-3.2%)
L	0.000	1.001 (-3.2%)	0.000

Table 5.6: Extracted coupling matrix of the manufactured model - silver/silver

materials	Q_0
aluminum/brass	1389
silver/brass	2498
silver/silver	3075

Table 5.7: Comparison of filter Q_0 estimates

initially constructed filter was poorly tuned, which is indicated by the high return loss in the center of the passband. Since the filter was later silver-plated, a repeated tuning and measurement was unfortunately not possible. To see the effects of this improvement, a

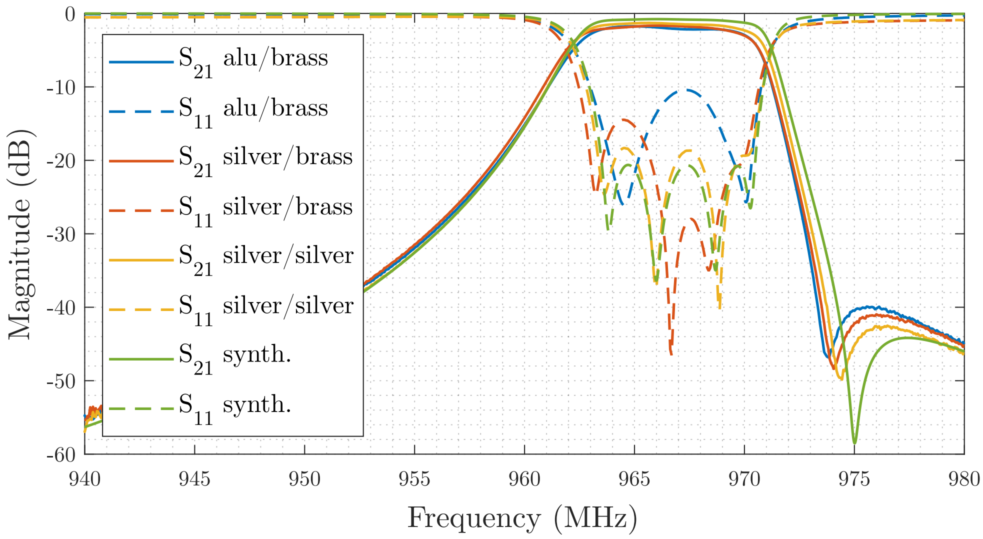

Figure 5.3: Comparison of tuned filter results for all material combinations

transmission loss comparison between all three material combinations and the synthesized design was made. How well the filter is tuned plays a big role in the passband transmission loss. Repeated equivalent tuning of all structures is practically impossible, so these effects have to be taken into account. Nevertheless, the overall improvement when the filter is silver-plated can be recognized from Figure 5.4. An estimated improvement of 0.5 dB is observed. The filter still does not reach the synthesized results, which were derived for a Q_0 of 3000. Presumably, the difference of approximately 0.5 dB, as estimated from the results, is due to additional connector losses and imperfect tuning. A larger transmission loss can be seen in the high end of the filter bandpass. This is due to the transmission zero, which was selected to be very close to the bandpass edge. An inconsistency between the CST simulated results, FD3D extracted results, and Equation (2.66) was observed. In Table 5.8, all three values for the example of a silver-plated cavity are listed. The simulation result is idealized, therefore it is expected to be higher than the realistic case. The value extracted from CST FD3D, however, should be similar to the calculated value from the empirical equation suggested by Hagensen. A more detailed analysis of the unloaded quality factor can only be done by realizing a single coaxial resonant cavity, which was out of scope for the work at hand.

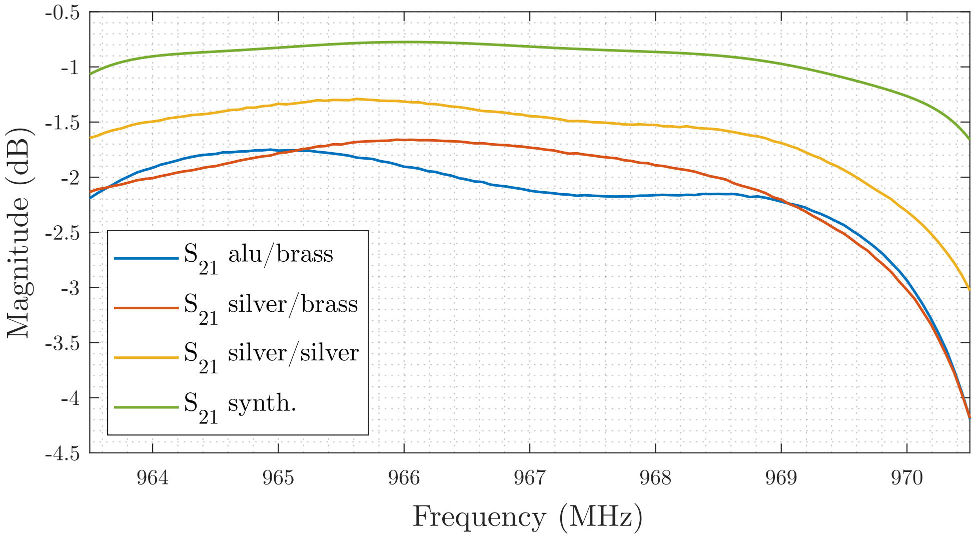

Figure 5.4: Transmission loss comparison between the three material combinations and the synthesized result

method	$\mathbf{Q_0}$
Hagensen [14]	1905
CST sim. post-proc. step	4422
CST FD3D extraction	3075

Table 5.8: Comparison of silver-plated Q_0 estimates: CST simulation vs. FD3D extraction vs. Hagensen

6 Conclusion and Outlook

The complete procedure of an RF bandpass filter design was presented in the course of this thesis. First, with the help of CST Filter Designer 3D, a coupling matrix was synthesized based on the design specifications. The coupling matrix coefficients were then realized by modeling tunable quarter-wavelength coaxial resonators and the mechanisms needed to realize external and interresonator couplings. The design and the choice of manufacturing materials were optimized for an in-house manufacturing. Hence, many design parameters were adopted to allow for a manufacturing process using machines with limited accuracy. The influences of all parameters were investigated by simulated parameter sweeps. During modeling, the limitations of the manufacturing process were kept in mind at all times. Critical parameters of the manufacturing process were identified. The modeled coupled resonator pairs from the simulation sweeps were then joined together to form a detuned four-resonator box-section filter. The filter had to be tuned by adapting the parameters with the use of previously obtained parameter sweep results. Based on the tuned simulation parameters, the filter was then produced in-house. Due to imperfections and numerical simulation errors, the measurement of the built filter was again detuned required a new tuning procedure, following the same sequential procedure as in the case of simulation results. As a final step, the filter was silver-plated to increase the unloaded Q-factor of the resonators, which is directly related to a reduction of the insertion loss. Since the insertion loss is highly dependent on the tuning quality, loss reduction conclusions cannot be made based on this. Q_0 was thus analyzed beforehand, by manufacturing individual resonant cavities. Two existing techniques for Q_0 evaluation were implemented for this analysis. Because the techniques do not consider coupling mechanism losses, the Q_0 factors were found to be inaccurate. Therefore, a new method for unloaded Q-factor evaluation of a single resonant cavity was proposed, which considers the losses and parasitic influences of the coupling mechanism and attempts to fit the results on a wide frequency band, contrary to the presented existing methods. To minimize the manufacturing errors, simple waveguide cavities were manufactured for this evaluation process instead of using the quarter-wavelength coaxial resonators. The impact of polishing was found to be negligible, while silver-plating resulted in a 33% increase of Q_0.

Again, it should be noted that the design and parameter selection here followed the limitations of the available manufacturing tools. Thus, the designed filter was optimized to the manufacturing process and not to maximum filter performance. Non-optimal materials with low, not precisely known electrical conductivity were used. Imprecision of the tools caused further deviations from the optimal design. For the evaluation of maximal possible filter performance, an optimal structure should be designed and manufactured instead. The filter tuning procedure has also proven itself as a difficult task. Methods to ease and speed up the tuning process of a filter should be further devised. Within the work done, an inconsistency between the experimental formula, simulation results and complete filter measurement estimation for the unloaded quality factor of a coaxial resonant cavity was found. To determine the validity of the three methods, this should be further investigated with the help of the introduced Q_0 estimation method.

After reading this document, the reader should be equipped with the know-how and theoretical background needed to design and manufacture a 3-D resonant cavity based filter. With the help of the evaluation of Q_0 improvement techniques, decisions regarding their implementation based on the filter specifications at hand can be drawn. The introduced Q_0 evaluation method is applicable on a wide range of EM resonant structures and can be used in various situations, where precise values of the unloaded Q-factor of a resonant cavity are required.

A Bandpass Filter Technical Drawings

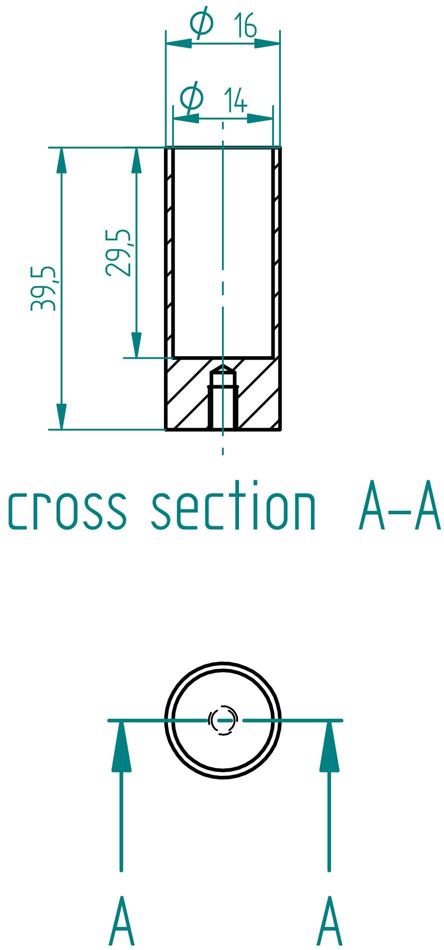

Figure A.1: Inner conductor dimensions

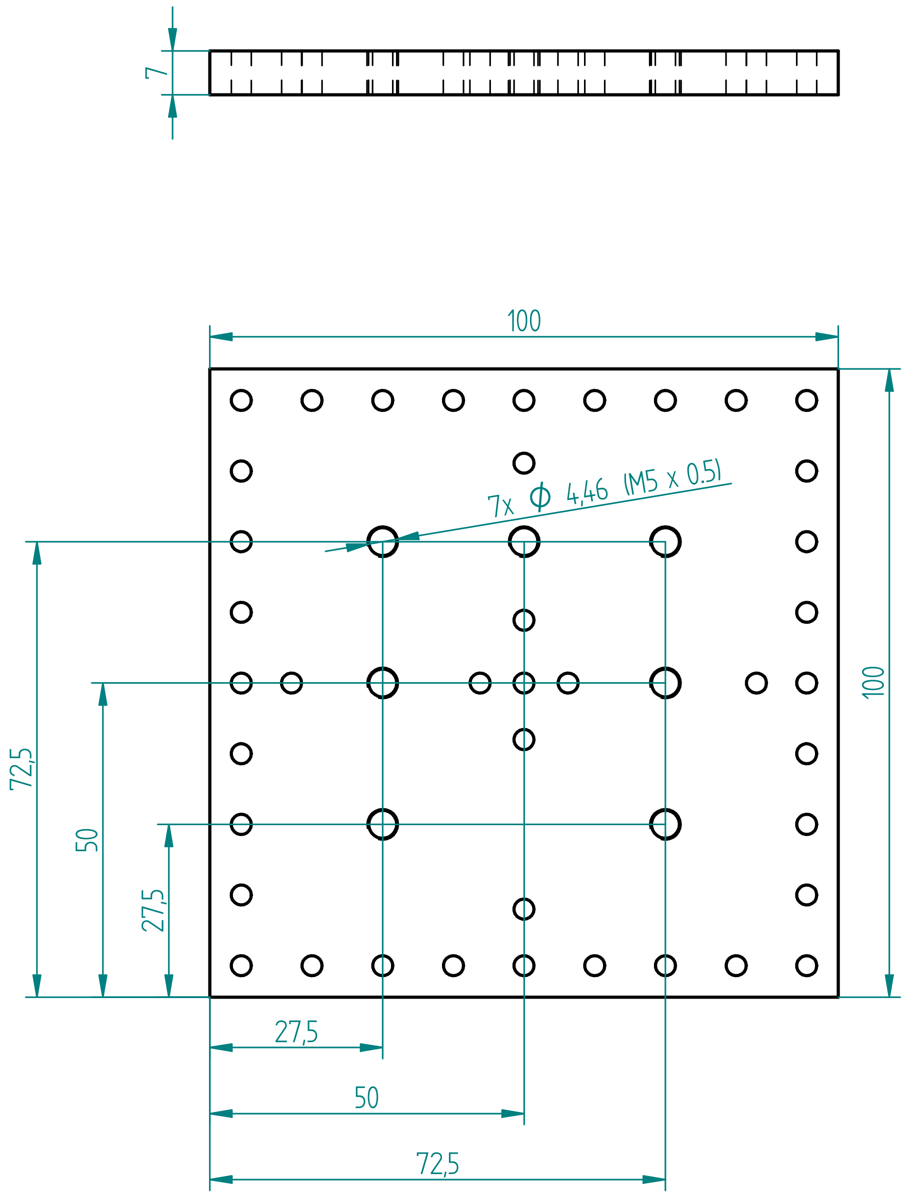

Figure A.2: Cover dimensions

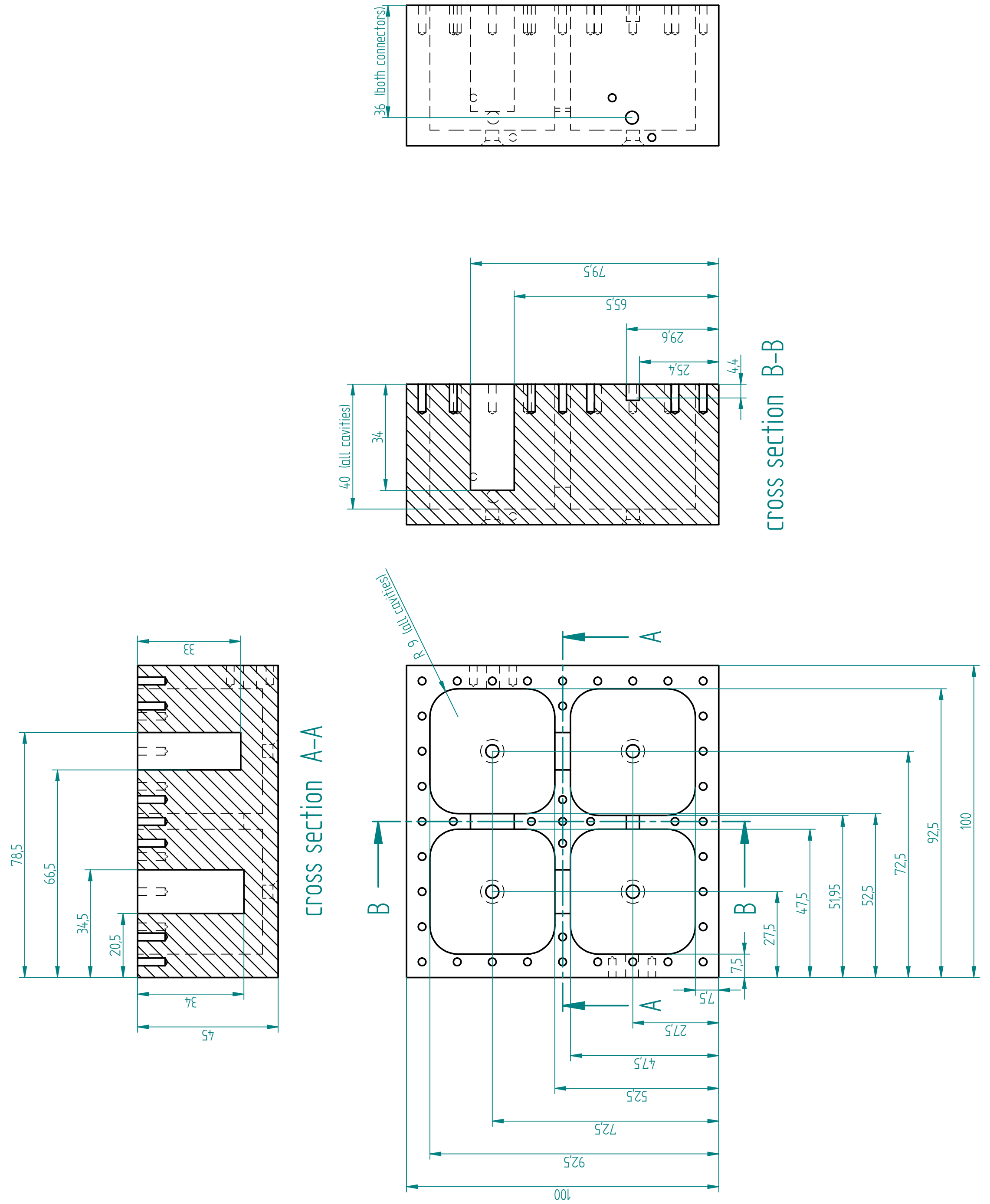

Figure A.3: Full filter dimensions

References

[1] R. J. Cameron, R. Mansour, and C. M. Kudsia. *Microwave Filters for Communication Systems: Fundamentals, Design and Applications.* Wiley, 2007. 1, 3, 4, 8, 15, 17, 19

[2] CST. CST Microwave Studio. `https://www.cst.com/products/cstmws`. 1, 14, 21

[3] D. Kajfez and E. J. Hwan. Q-Factor Measurement with Network Analyzer. *IEEE Transactions on Microwave Theory and Techniques*, 32(7):666–670, Jul 1984. 2, 8, 50, 52, 53

[4] D. M. Pozar. *Microwave Engineering, 4th Edition.* Wiley, 2011. 4, 5, 6, 8

[5] C. G. Montgomery. *Technique of microwave measurements.* Radiation Laboratory series. McGraw-Hill Book Co., 1947. 4

[6] R. Collin. *Foundations for microwave engineering.* IEEE Press, New York, 2001. 5

[7] J. S. Hong. Couplings of asynchronously tuned coupled microwave resonators. *IEE Proceedings - Microwaves, Antennas and Propagation*, 147(5):354–358, Oct 2000. 7, 8

[8] J. S. Hong and M. J. Lancaster. *Microstrip Filters for RF / Microwave Applications.* Wiley Series in Microwave and Optical Engineering. Wiley, 2001. 8

[9] E. L. Ginzton. *Microwave measurements.* International series in pure and applied physics. McGraw-Hill, 1957. 8

[10] S. Shahid, J. A. R. Ball, C. G. Wells, and P. Wen. Reflection type Q-factor measurement using standard least squares methods. *IET Microwaves, Antennas Propagation*, 5(4):426–432, Mar 2011. 11, 47, 48, 50, 52, 53

[11] I. Kåsa. A circle fitting procedure and its error analysis. *IEEE Transactions on Instrumentation and Measurement*, IM-25(1):8–14, Mar 1976. 11

[12] G. Gold and K. Helmreich. A physical model for skin effect in rough surfaces. In *2012 42nd European Microwave Conference*, pages 1011–1014, Oct 2012. 13

[13] G. Gold and K. Helmreich. Effective conductivity concept for modeling conductor surface roughness. *DesignCon 2014*, pages 1–21, Jan 2014. 13

[14] M. Hagensen. Narrowband Microwave Bandpass Filter Design by Coupling Matrix Synthesis. *Microwave Journal*, 0(4), Apr 2010. 21, 56

[15] J. B. Thomas. Cross-coupling in coaxial cavity filters - a tutorial overview. *IEEE Transactions on Microwave Theory and Techniques*, 51(4):1368–1376, April 2003. 22, 23

[16] MathWorks. MATLAB. `https://www.mathworks.com/products/matlab.html`. 37

[17] J. Paleček, M. Vestenický, P. Vestenický, and J. Spalek. Examination of SMA connector parameters. In *2012 IEEE 16th International Conference on Intelligent Engineering Systems (INES)*, pages 259–263, June 2012. 47

[18] National Instruments. NI AWR Microwave Office. `https://www.awrcorp.com/products/ni-awr-design-environment/microwave-office-software`. 48

Hiermit erkläre ich, dass die vorliegende Arbeit gemäß dem Code of Conduct – Regeln zur Sicherung guter wissenschaftlicher Praxis (in der aktuellen Fassung des jeweiligen Mitteilungsblattes der TU Wien), insbesondere ohne unzulässige Hilfe Dritter und ohne Benutzung anderer als der angegebenen Hilfsmittel, angefertigt wurde. Die aus anderen Quellen direkt oder indirekt übernommenen Daten und Konzepte sind unter Angabe der Quelle gekennzeichnet.
Die Arbeit wurde bisher weder im In– noch im Ausland in gleicher oder in ähnlicher Form in anderen Prüfungsverfahren vorgelegt.

Wien, 16. November 2018 *Jure Soklič*